Synthesis and photocatalytic properties of novel nanostructured pyrochlores from Bi_2O_3-Fe_2O_3-Nb_2O_2 and Bi_2O_2-Fe_2O_3-TeO_2 systems

Metka Benčina

Materials Research Laboratory, University of Nova Gorica, Vipavska 13, SI-5000 Nova Gorica

Abstract

Pure phase $Bi_{1.647}Nb_{1.118}Fe_{1.157}O_7$ and $Bi_{1.9}Te_{0.58}Fe_{1.52}O_{6.87}$ nanoparticles were for the first time successfully synthesized by co-precipitation method and further thermal treatment. The as-prepared nanopowders, characterized by X-ray diffraction (XRD) and scanning electron microscope (SEM) exhibited a pure pyrochlore phase, $Bi_{1.647}Nb_{1.118}Fe_{1.157}O_7$ consisting of spherical particles with dimensions of about 40-60 nm and $Bi_{1.9}Te_{0.58}Fe_{1.52}O_{6.87}$ with dimensions of about 30-60 nm. Diffuse reflectance spectroscopy in visible and UV light range indicated that these nanoparticles absorb a wider wavelength range of visible light than $Bi_2Ti_2O_7$. Photocatalytic studies under visible light irradiation toward the decomposition of methyl orange solution with addition of hydrogen peroxide revealed that novel nanoparticles possess excellent photocatalytic properties, even better than $Bi_2Ti_2O_7$ and commercial TiO_2 - P25.

Keywords: pyrochlores, nanoparticles, photocatalysis, dye degradation

1. Introduction

The large band gap energy of widely studied TiO_2 (3.2 eV for commercial P25) restrains its use under visible light irradiation. It is well known that visible region occupies 45 % of solar spectrum, while less than 5 % belongs to UV light [1], which makes the development of more suitable semiconductor photocatalysts an indispensable and an imperative topic in material science. Several challenges in developing of visible-light driven

Email address: metka.bencina@ung.si (Metka Benčina)

semiconductor photocatalysts remain as yet unsolved, such as low absorption of visible light, low mobility of generated electrons and holes and high recombination rate. Electron-hole pairs can be generated by photons with energies greater than the band gap of the material in question. Due to high high demand of visible light sensitive photocatalysts, one of necessary conditions is narrow enough band gap.

The compositional flexibility of pyrochlores ($A_2B_2O_6O$; A, B represent metals) offers the ability to manipulate properties of the engineered material, that can be harnessed in a search for new photocatalysts, applicable for the visible light. The band gap reduction caused by the upward shift of the valence band due to Bi 6s or hybrid Bi 6s - O 2p orbitals has been shown in bismuth titanate [2]. $Bi_2Ti_2O_7$ is a promising photo-active member of the pyrochlore family and several studies about its synthesis and photocatalytic properties [2-13] and density functional theory (DFT) studies [14-16] have been published. DFT studies, performed by Murugesan *et al.* [14] showed that substitution in $Bi_2Ti_2O_7$ with 3d transition metal, such as Fe, leads to generating interband states between valence and conduction band, which lead to reducing the band gap. Valant *et al.* [17] proposed Bi_2O_2-Fe_2O_3-TeO_2 pyrochlores as possible visible light driven photocatalysts. The same authors also experimentally showed that Fe significantly reduces band gap of the material [17]. Stoichiometric compounds from Bi_2O_3-Fe_2O_3-Nb_2O_2 system were synthesized by solid-state reaction as well [18], but, to the best of our knowledge, no photocatalytic properties of these materials have been tested to date.

Here, we report on the synthesis and the photocatalytic properties of new nanoparticles from Bi_2O_3-Fe_2O_3-Nb_2O_2 and Bi_2O_2-Fe_2O_3-TeO_2 systems in comparison with $Bi_2Ti_2O_7$ nanoparticles and commercial TiO_2 - P25.

2. Experimental details

2.1. Chemicals used in the synthesis and photocatalytic activity experiments

The following chemicals were used in the experiments: Bismuth (III) nitrate pentahydrate (Alfa Aesar, 98%), iron (III) nitrate nonahydrate (Alfa Aesar, 98+%), niobium (V) chloride (Alfa Aesar, 99.9%), acetic acid (Sigma Aldrich, 99.7%), absolute ethanol (Sigma Aldrich, 99.8%), NH_4OH (Fluka, 25%), tellurium powder (60 mesh, Alfa Aesar, 99.999%), nitric acid (Fluka, 65%), bismuth (III) oxide (Alfa Aesar, 99,975%), niobium (V) oxide (Alfa Aesar, 99,975%), tellurium (III) oxide (Alfa Aesar, 99,99%), iron (III) oxide (Alfa Aesar, 99,945%), titanium (IV) isopropoxide (Alfa Aesar, 97%), methyl

orange (Alfa Aesar, ACS), hydrogen peroxide (Belinka Perkemija, 30%) and Aeroxide®P25 TiO_2 (Degussa, Evonik, Sigma Aldrich, 99.5%).

2.2. Synthesis

Bismuth (III) nitrate pentahydrate, iron (III) nitrate nonahydrate and niobium (V) chloride were used as precursor materials for preparation of nanoparticles from Bi_2O_3-Fe_2O_3-Nb_2O_2 system. The stoichiometric amounts of precursors were dissolved in acetic acid and absolute ethanol and the solution was alkalized with NH_4OH. Niobium chloride was taken out from the packing and put into the glass vial with known mass inside the glovebox. The vial containing the chemical was then weighted again and the mass of niobium chloride was calculated from the difference in weight. Absolute ethanol (5 ml) was poured inside the vial using the syringe and needle in order to dissolve niobium chloride. The solution was transferred to the 100 ml baker and stirred with magnetic stirrer for 10 min. Bismuth nitrate was placed in the 100 ml baker and dissolved in acetic acid (20 ml) after 20 min of stirring by a magnetic stirrer. Iron nitrate was later added to the bismuth nitrate solution followed by 5 min of stirring. The solution of niobium chloride was added to the solution of dissolved bismuth and iron nitrate and stirred for another 10 min. The NH_4OH was added to the solution until the pH was 8. A pale orange precipitate was filtered under vacuum and filter paper with pore size of approximately 2-3 μm. After vacuum filtering and washing with abundant of deionized water and ethanol with intermediate centrifuging for several times, the powder was dried at 100 °C for approximately 3 h. Then, the powder was slightly ground in an agate mortar and annealed in an aluminium oxide crucible in air atmosphere at 570 °C for 15 h.

The synthesis of the Bi_2O_2-Fe_2O_3-TeO_2 samples followed similar procedure with only few changes; Tellurium powder was used instead of niobium (V) chloride and acetic acid and absolute ethanol were replaced by nitric acid 25 ml. Stoichiometric amounts of bismuth nitrate, iron nitrate and tellurium powder were used. As-prepared powder was annealed in an aluminium oxide crucible in air atmosphere at 570 °C for 15 h.

Additionally, $Bi_2Ti_2O_7$ nanoparticles were prepared by co-precipitation method [7]. Bismuth (III) nitrate pentahydrate and titanium (IV) isopropoxide were used as starting materials. Acetic acid was used as a solvent. The solution was alkalized with ammonium hydroxide (NH_4OH). Bismuth nitrate was dissolved in acetic acid after 20 min of stirring by a magnetic stirrer in a 100 ml baker. Titanium isopropoxide (an excess of 23 % related to bismuth nitrate to obtain a pure $Bi_2Ti_2O_7$ phase [3]) was then poured into

the solution and stirred for another 5 min. Solution was stable as both precursors were completely soluble. NH_4OH was added into the solution very slowly, drop by drop, inside a fume hood with continuous stirring. At pH = 7 white precipitate was formed, which was vacuum filtered by filter paper with pore size of approximately 23 μm, washed with deionized water and dried at 100 °C for 3 h. Then, the powder was slightly ground in an agate mortar and annealed in an aluminium oxide crucible in air atmosphere at 540 °C for 16 h.

2.3. Characterization

Phase identification was performed by using XRD using PAN-alytical X'pert pro MPD [1] in BraggBrentano geometry using Cu K-alpha radiation over the range 5° to 90° 2Θ with a step size of 0.017° 2Θ, divergence slit of 0.218 ° 2Θ, counting step time of 25 s and continuous scanning mode. Diffuse reflectance spectra (UV-vis) were measured with a PerkinElmer Lambda 650S [2] spectrophotometer on powder samples in 250-700 nm spectral range. A Spectralon reflection standard was used as a reference. Band gaps energies (E_g) were determined by plotting absorbance in Kubelka-Munk function versus energy. SEM images were obtained on a Zeiss SUPRA-40 instrument with Schottky field emission. The samples were scanned at an voltage of 10 kV.

2.4. Photocatalytic tests

Photocatalytic activity was evaluated by the degradation of methyl orange (MO) in aqueous solutions using a custom-made photoreactor, utilizing four visible 60 W lamps [3] and six 18 W UV lamps [4] (Figure 1). The photoreactor walls were made from highly reflective Al-foil [5] in order to provide as far as possible luminous efficacy. The photoreactor's cell was cooled with tap water. The temperature of the reaction mixture during the tests was 12 ° C. Under the cell the magnetic stirrer was placed in order to maintain the reaction mixture homogenous. Due to band gap values, the photocatalytic activity measurements were carried out under visible light. 0.1 g of photocatalyst was placed in 75 ml MO solution with an initial concentration of 14.2 mg/l and 4 ml H_2O_2. Before illumination, the

[1] Almelo, Netherlands
[2] Waltham, MA, USA
[3] Osram 60W S-14S Linestra, Germany
[4] Osram FD T26 L18W-73 G13 BLB Black light UV, Germany
[5] Intra lighting d.o.o., Slovenia

mixture was exposed to ultrasound for 15 min in the dark in order to establish adsorption-desorption equilibrium between the dye and the photocatalyst. The mixture was stirred during the irradiation. At a given irradiation time intervals, 3 ml aliquots were taken from the reaction suspension by syringe. The samples were centrifuged for 20-30 min with 10000 rpm in order to remove photocatalyst and additionally filtered in order to remove dust and impurities by using syringe filters with pore size of 0.2 μm. The absorbance of supernatant MO solutions was then measured with Perkin Elmer Lambda 650s spectrophotometer.

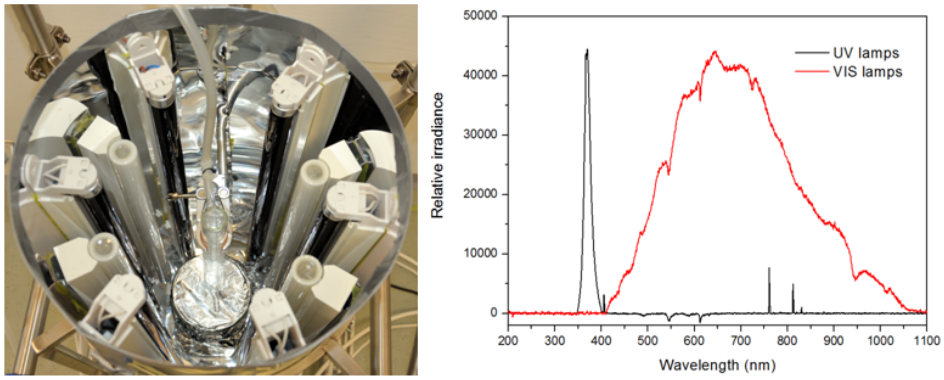

Figure 1: Custom-made photoreactor containing 6 UV and 4 visible lamps (left) and their corresponding spectrum (right). In the presented research only the irradiation with visible lamps was used.

3. Results and discussion

3.1. Phase structures and morphology

Phase purity and crystallite size are key parameters of our target materials, so the first step of characterization of the prepared powders is their XRD analysis. Coprecipitation reaction followed by annealing of the powder at 570 °C for 15 h was found to result in pure phase $Bi_{1.647}Nb_{1.118}Fe_{1.157}O_7$ and $Bi_{1.9}Te_{0.58}Fe_{1.52}O_{6.87}$ nanoparticles with pyrochlore structure (Figure 2). $Bi_2Ti_2O_7$ nanoparticles, also shown in Figure 2, prepared by the coprecipitation method and annealed at 540 °C for 16 h, exhibit single-phase pyrochlore structure as well. Well defined sharp peaks indicate that materials consist of highly crystallized nanoparticles. The crystallite size was calculated from the XRD diffraction line broadening using Scherrer's formula [19] (Table 1). Predicted crystallite sizes of the $Bi_{1.647}Nb_{1.118}Fe_{1.157}O_7$

and $Bi_{1.9}Te_{0.58}Fe_{1.52}O_{6.87}$ nanoparticles were found to be in good agreement with the particle sizes determined from SEM (40-60 nm and 30-60 nm, respectively). SEM analysis revealed that $Bi_{1.647}Nb_{1.118}Fe_{1.157}O_7$ and $Bi_{1.9}Te_{0.58}Fe_{1.52}O_{6.87}$ nanoparticles were spherically shaped and slightly agglomeratated (Figure 3).

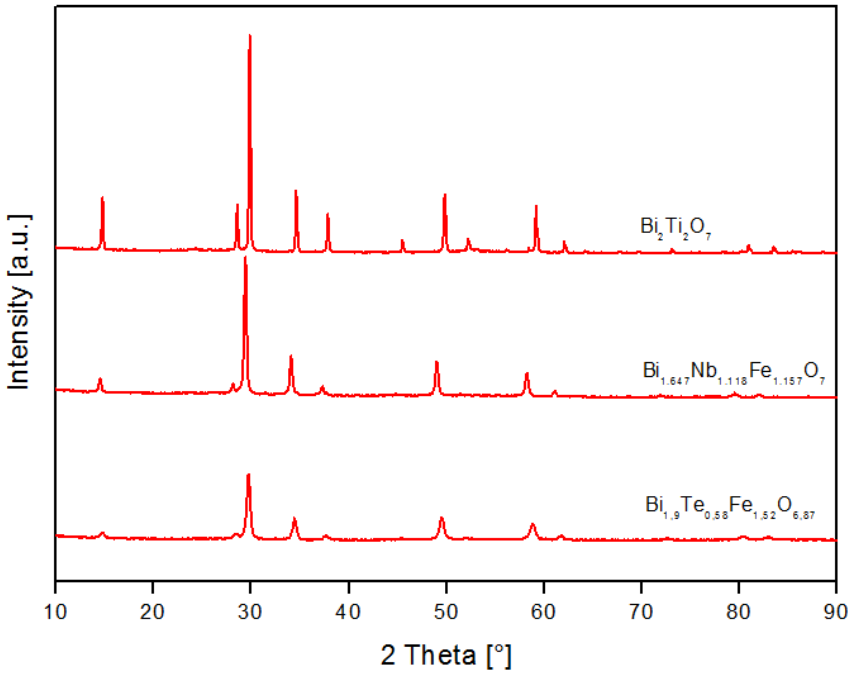

Figure 2: X-ray diffraction patterns of pure phase $Bi_2Ti_2O_7$, $Bi_{1.647}Nb_{1.118}Fe_{1.157}O_7$ and $Bi_{1.9}Te_{0.58}Fe_{1.52}O_{6.87}$ structured pyrochlores. Broad peaks confirm the presence of nanoparticles.

Esquivel-Elizondo *et al.* [3] discussed difficulties in preparing stoichiometric $Bi_2Ti_2O_7$, which is often synthesized with a $Bi_4Ti_3O_{12}$ by-phase. They showed perfect agreement between DFT studies and experimentally obtained XRD pattern indicating single phase purity of $Bi_2Ti_2O_7$. Besides XRD analysis, an easy estimation of the purity of the powder is by its colour; with increasing amount of secondary phases the colour turns from white to yellow and finally to orange [3]. In this work we obtained white $Bi_2Ti_2O_7$ nanoparticles, which confirmed the presence of only one phase in the powder.

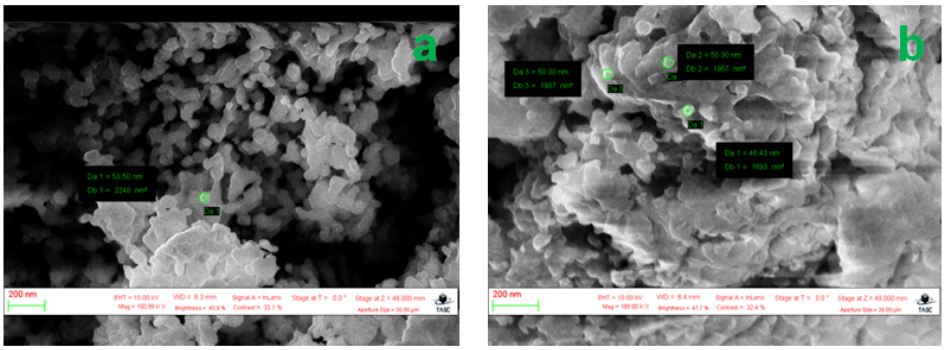

Figure 3: SEM micrographs showing spherical shape of (a) $Bi_{1.647}Nb_{1.118}Fe_{1.157}O_7$ and (b) $Bi_{1.9}Te_{0.58}Fe_{1.52}O_{6.87}$ nanoparticles (scale bar represents 200 nm).

3.2. *Analysis of the diffuse reflectance spectrum*

The materials that are supposed to be used in photocatalytic application, have to absorb the appropriate wavelength of light. Spectroscopic measurements in UV-visual part of the spectrum of $Bi_{1.647}Nb_{1.118}Fe_{1.157}O_7$ and $Bi_{1.9}Te_{0.58}Fe_{1.52}O_{6.87}$ nanoparticles showed that the maximum absorption wavelength is red-shifted compared to TiO_2 and $Bi_2Ti_2O_7$ (Figure 4), which means that these particles are able to absorb more visible light. Since the sizes of $Bi_{1.647}Nb_{1.118}Fe_{1.157}O_7$, $Bi_{1.9}Te_{0.58}Fe_{1.52}O_{6.87}$ and $Bi_2Ti_2O_7$ nanomaterials are approximately in the same range, and also their preparation methods are the same, our conclusion is that substitution of Ti^{4+} by Fe^{3+} and Nb^{5+} or Te^{5+} ions contributes to the shift of the absorption edge. Extracted indirect and direct band gap energies using the Kubelka-Munk function also revealed the great potential of the prepared nanoparticles for the visible light photoactivity (Table 1).

Theoretical calculations performed by Murugesan *et al.* [14] suggest that $Bi_2Ti_2O_7$ pyrochlore is a direct band gap material with band width of 2.6 eV, but experimentally obtained band gap of same material nanostructure has a value of 2.88 eV, which is about 0.4 eV lower compared to TiO_2 in anatase form (band gap of 3.20 eV). Yao *et al.* [10] reported indirect band gap of $Bi_2Ti_2O_7$ (200-800 nm in size) to be 2.95 eV, but XRD pattern clearly shows existence of secondary phases. In the present study we obtained the following: direct band gap of 3.18 eV and indirect band gap of 2.47 eV for $Bi_2Ti_2O_7$ pyrochlore nanoparticles (Table 1). The band gaps of the Bi_2MNbO_7 (M = Al^{3+}, Ga^{3+} or In^{3+}) were estimated to be 2.9 eV, 2.75 eV and 2.7 eV, respectively [20]. The same authors claim that the band gap of Bi_2FeNbO_7 is about 2.1 eV, while Garza-Tovar *et al.* [21] found the band gap

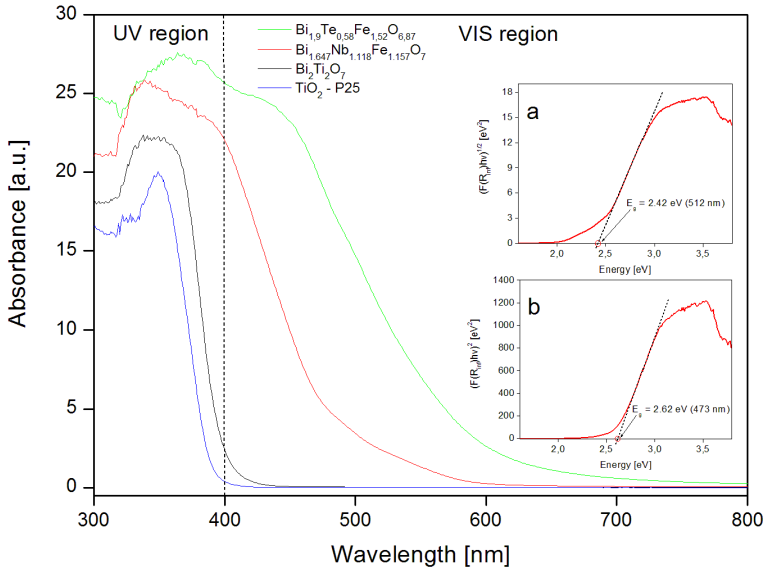

Figure 4: UV-Vis diffuse reflectance spectra of obtained $Bi_2Ti_2O_7$, $Bi_{1.647}Nb_{1.118}Fe_{1.157}O_7$ and $Bi_{1.9}Te_{0.58}Fe_{1.52}O_{6.87}$ nanoparticles. The inset shows the indirect (a) and direct (b) band gap determination of $Bi_{1.647}Nb_{1.118}Fe_{1.157}O_7$ nanoparticles.

of same material to be 1.9 eV (calcined at 600 °C) and 1.75 eV (calcined at 800 °C). The research of Lufaso *et al.* [18] showed that the materials with the composition Bi_2FeNbO_7 does not exist, but rather stoichiometries that are Bi deficient are formed. To the best of our knowledge, no optoelectronic studies were performed on these materials. Valant *et al.* [17] determined direct band gaps of $(Bi_2\text{-}xFex)(Fe_{1.42}Te_{0.58})O_{6.87}$ (x = 0.007, 0.14, 0.21) to be 2.078 eV, 2.075 eV and 1.965 eV for x = 0.007, 0.14, 0.21, respectively, and among them the band gap of 1.965 eV is so far the lowest band gap reported for Bi containing pyrochlores. That work confirmed the prediction that choosing the Fe to be part of B side within pyrochlore structure leads to the decrease in the band gap. They chose the direct band gaps as more plausible because plots of $|F(R)h\nu|^2$ vs. E showed linear regions [17]. In our case, both, plots of $|F(R)h\nu|^2$ vs. E and $|F(R)h\nu|^{1/2}$ vs. E show linear regions (Figure 4).

The direct band gap values determined in present work are higher than values reported by Valant *et al.* [17], while values of indirect band gaps are

Table 1: Examined band gaps (E_g) (direct and indirect) and crystallite sizes determined from XRD patterns of phase pure nanostructured pyrochlores. It is clearly seen that the replacement of Ti by Fe and Te/Nb ions can efficiently reduces band gap.

Material	Dir. E_g (eV)	Ind. E_g (eV)	Crystallite size (nm)
$Bi_2Ti_2O_7$	3.18	2.47	30 - 90
$Bi_{1.647}Nb_{1.118}Fe_{1.157}O_7$	2.62	2.42	30 - 60
$Bi_{1.9}Te_{0.58}Fe_{1.52}O_{6.87}$	2.32	1.76	20 - 50

much more comparable with values of direct band gaps estimated within their research. For example, the direct and indirect band gaps of the material with $Bi_{1.8}Fe_{1.55}Te_{0.65}O_{6.98}$ composition are 2.47 eV and 1.92 eV, respectively [17]. According to the reported general formula (Bi_2-xFex)($Fe_{1.42}$-$Te_{0.58}$)$O_{6.87}$) [17], the x value of our composition is 0.2. The published band gap for material with x = 0.21 is 1.965 eV [17]. It is worth to note, that band gaps of bulk materials are lower than those of nanomaterials due to quantum size effect. But, since there are no standard ways to determine which kind of electron transition is more plausible in the materials, we continue to investigate the electronic structure to understand the real nature of the band gap.

3.3. Photocatalytic properties

Photocatalytic activity of the as-prepared materials was determined by examination of MO degradation, since MO solution can demonstrate an artificial textile wastewater. Decrease of intensity of maximum absorption peak of MO at 464 nm was examined. $Bi_{1.647}Nb_{1.118}Fe_{1.157}O_7$ and $Bi_{1.9}Te_{0.58}$-$Fe_{1.52}O_{6.87}$ nanoparticles individually are not highly photocatalytically active under visible light, since they do not induce rapid MO degradation, therefore, H_2O_2 was introduced into the mixture containing nanoparticles and 75 ml 14,2 mg/l MO solution. H_2O_2 not only has the role of photoelectron acceptor and agent that prevents recombination between photogenerated electrons and holes, it also generates strongly oxidizing OH radicals, which can lead to further increase of degradation rate [22]. By using visible light, MO was degraded almost completely after 8 h in the presence of $Bi_{1.647}Nb_{1.118}Fe_{1.157}O_7$ nanoparticles (Figure 5 and 6), which suggests a remarkable enhancement of photocatalytic activity.

In comparison, $Bi_{1.9}Te_{0.58}Fe_{1.52}O_{6.87}$ and $Bi_2Ti_2O_7$ nanoparticles lead to approximately the same degradation rate of MO and it can be seen from

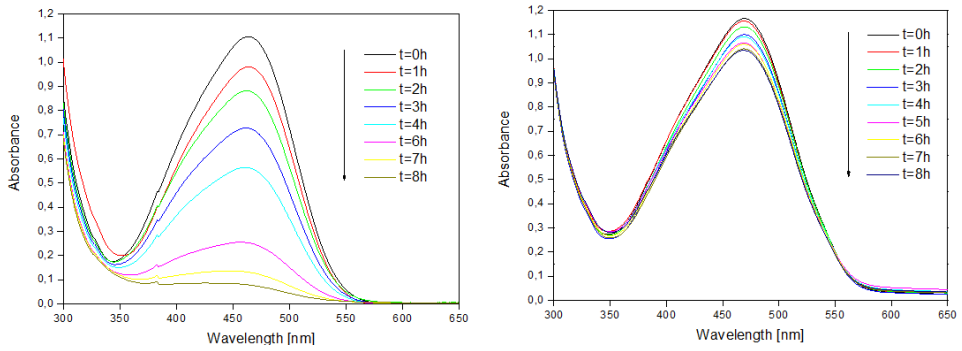

Figure 5: Temporal evolution of the absorption spectrum of MO solution (14,2 mg/l) in the presence of 4 ml H_2O_2 and $Bi_{1.647}Nb_{1.118}Fe_{1.157}O_7$ nanoparticles (left) or P25 TiO_2 (right). Degradation of MO is faster by using $Bi_{1.647}Nb_{1.118}Fe_{1.157}O_7$ nanoparticles as a photocatalyst, than P25 TiO_2.

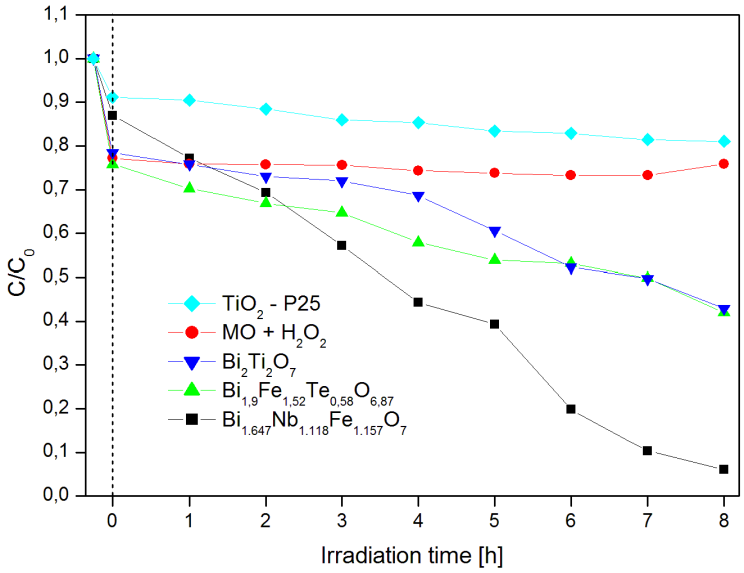

Figure 6: Kinetics of the photocatalytic degradation of MO solution (14.2 mg/l) with addition of H_2O_2 to photocatalysts under visible-light irradiation.

Figure 5 that they are not so efficient as $Bi_{1.647}Nb_{1.118}Fe_{1.157}O_7$ nanoparticles. In order to exclude the possibility of dye photolysis induced by the

presence of H_2O_2, test without photocatalyst was performed under visible light. As one can see from Figure 6, the degradation of MO in that test was very slow. In comparison, photocatalytic activity of TiO_2 - P25 was tested by using the same conditions as in previous tests. The degradation of MO under visible light was very slow as well.

4. Conclusions

Phase pure $Bi_{1.647}Nb_{1.118}Fe_{1.157}O_7$ and $Bi_{1.9}Te_{0.58}Fe_{1.52}O_{6.87}$ nanoparticles having pyrochlore structure were synthesized by co-precipitation reaction and thermal treatment in the furnace at 570 °C for 15 h for the first time. Both as-synthesized nanomaterials exhibit much higher photocatalytic activity under visible light than commercially obtained P25 TiO_2 in the presence of H_2O_2. $Bi_{1.647}Nb_{1.118}Fe_{1.157}O_7$ nanoparticles showed excellent photocatalytic activity under visible light, since the dye (MO) degraded almost completely after 8 h. Photocatalytic activity of $Bi_{1.9}Te_{0.58}Fe_{1.52}O_{6.87}$ and $Bi_2Ti_2O_7$ nanoparticles is lower than of $Bi_{1.647}Nb_{1.118}Fe_{1.157}O_7$ nanoparticles, but much higher than of P25 TiO_2. Further dye degradation studies and also tests for H_2 evolution by using these novel nanoparticles are under way.

5. Acknowledgements

This work was financially supported by the Slovenian Research Agency under the young researcher grant. We wish to thank to dr. Mattia Fanetti for his help with SEM measurements.

References

[1] Y. Fu, X Wang. *Magnetically Separable ZnFe2O4-Graphene Catalyst and its High Photocatalytic Performance under Visible Light Irradiation.* Industrial & Engineering Chemistry Research, 50, 12: 7210-7218, 2011.

[2] S. Murugesan, V.(R). Subramanian. *Robust synthesis of bismuth titanate pyrochlore nanorods and their photocatalytic applications.* Chemical Communications, 34: 5109-5111, 2009.

[3] J.R. Esquivel-Elizondo, B.B. Hinojosa, J.C. Nino. *$Bi_2Ti_2O_7$: It Is Not What You Have Read.* Chemistry of Materials, 23, 22: 4965-4974, 2011.

[4] H. Zhou, T-J. Park. *Synthesis, characterization, and photocatalytic properties of pyrochlore $Bi_2Ti_2O_7$ nanotubes.* Journal of Materials Research, 21, 11: 2941-2947, 2006.

[5] J. Hou, S. Jiao, H. Zhu, R.V. Kumar. *Bismuth Titanate Pyrochlore Microspheres: Directed Synthesis and Their Visible Light Photocatalytic Activity.* Journal of Solid State Chemistry, 184, 1: 154-158, 2011.

[6] X. Su, Y. Zhang. *Synthesis and Photocatalytic Properties of $Bi_2Ti_2O_7$ Nano-Powders.* Advanced Materials Research, 412: 103-106, 2011.

[7] W.F. Su, Y.T. Lu. *Synthesis, phase transformation and dielectric properties.* Materials Chemistry and Physics, 80: 632-637, 2003.

[8] J. Ren, G. Liu, Y. Wang, Q. Shi. *A novel method for the preparation of $Bi_2Ti_2O_7$ pyrochlore.* Materials Letters, 76: 184-186, 2012.

[9] A.L. Hector, S.B. Wiggin. *Synthesis and structural study of stoichiometric $Bi_2Ti_2O_7$ pyrochlore.* Journal of Solid State Chemistry, 177, 1: 139-145, 2004.

[10] W.F. Yao, H. Wang , X.H. Xu, J.T. Zhou, X.N. Yang , Y. Zhang , S.X. Shang. *Photocatalytic property of bismuth titanate $Bi_2Ti_2O_7$.* Applied Catalysis A: General, 259, 1: 29-33, 2004.

[11] S.P. Yordanov, I. Ivanov , C.P. Carapanov. *Dielectric properties of the ferroelectric ceramics.* Journal of Physics D: Applied Physics, 31, 7: 800-806, 1998.

[12] V. Parvanova. *Synthesis and thermal decomposition of bismuth peroxotitanate to $Bi_2Ti_2O_7$.* Journal of Thermal Analysis and Calorimetry, 86, 2: 443-447, 2006.

[13] Y. Hou, M. Wang, X-H. Xu, D. Wang, H. Wang, S-X. Shang. *Dielectric and Ferroelectric Properties of Nanocrystalline $Bi_2Ti_2O_7$ Prepared by a Metallorganic Decomposition Method.* Journal of the American Ceramic Society, 85, 12: 3087-3089, 2002.

[14] S. Murugesan, M.N. Huda, Y. Yan, M.M. Al-Jassim, V.(R.). Subramanian. *Band-Engineered Bismuth Titanate Pyrochlores for Visible Light Photocatalysis.* The Journal of Physical Chemistry, 114: 10598-10605, 2010.

[15] B.B. Hinojosa, J.C. Nino, A. Asthagiri. *First-principles study of cubic Bi pyrochlores.* Physical Review B 77, 10: 104123, 2008.

[16] W. Wei, Y. Dai , B. Huang. *First Principle Characterization of Bi-based Photocatalysts: $Bi_{12}TiO_{20}$, $Bi_2Ti_2O_7$ and $Bi_4Ti_3O_{12}$*. The Journal of Physical Chemistry C, 113, 14: 5658-5663, 2009.

[17] M. Valant, G.S. Babu, M. Vrcon, T. Kolodiazhnyi, A-K. Axelsson. *Pyrochlore Range from Bi_2O_2-Fe_2O_3-TeO_2 System for LTCC and the Crystal Structure of New $Bi_3(Fe_{0.56}Te_{0.44})_3O_{11}$*. Journal of the American Ceramic Society, 95, 2: 644-650, 2011.

[18] M.W. Lufaso, T.A. Vanderah, I.M. Pazos , I. Levin , R.S. Roth ,J.C. Nino, V. Provenzano ,P.K. Schenck. *Phase formation, crystal chemistry, and properties in the system Bi_2O_3-Fe_2O_3-Nb_2O_2.* Journal of Solid State Chemistry, 179, 12: 3900-3910, 2006.

[19] A.L. Patterson. *The Scherrer Formula for X-Ray Particle Size Determination.* Physical Review, 56, 10: 978-982, 1939.

[20] Z. Zou,J. Ye,H. Arakawa. *Photocatalytic and photophysical properties of a novel series of solid photocatalysts, Bi_2MNbO_7 (M=Al^{3+},Ga^{3+} and In^{3+})* Chemical Physics Letters, 333, 1: 57-62, 2001.

[21] L.L. Garza-Tovar, L.M. Torres-Martnez, D.B. Rodrguez, R. Gmez, G. del Angel. *Photocatalytic degradation of methylene blue on Bi_2MNbO_7 (M = Al, Fe, In, Sm) solgel catalysts* Journal of Molecular Catalysis A: Chemical, 247, 1-2: 283-290, 2006.

[22] J.Q. Chen, D. Wang, M.X. Zhu, C.J. Gao. *Study on degradation of methyl orange using pelagite as photocatalyst* Journal of Hazardous Materials B 138: 182186, 2006.

Photocatalytic and structural properties of titania/mesoporous silica composites immobilized on glass

Andraž Šuligoj

Laboratory for Environmental Research, University of Nova Gorica, Vipavska 13, 5001 Nova Gorica, Slovenia

Abstract

Photocatalytically active TiO_2 and TiO_2/SiO_2 thin layers were successfully synthesized by low temperature sol-gel method and immobilized on glass slides. They were characterized using SEM, XRD, BET, FT-IR and their photocatalytic activity was tested towards degrading airborne toluene in a carberry-type photoreactor. Photocatalytic and adsorption properties of the catalysts were improved by incorporating titania into pores of ordered (SBA-15) and disordered (KIL-2) mesoporous silica. The addition of silica resulted in a smaller crystal size of titania and thus a higher surface area. The latter was found to be an important property influencing the final photocatalytic activity of the material.

Keywords: Mesoporous silica, TiO_2 photocatalysis, Toluene, Air remediation

1. Introduction

It is estimated that today people in developed countries spend more than 80 % of their time indoors [1]. One of the main indoor air pollutants are volatile organic compounds (VOCs), of which the most occurring species include ethanol, limonene, acetone, toluene and methylene chloride. The concentration of individual VOC is usually between 5 to 50 $\mu g/m^3$, while the total concentrations of VOCs are usually much higher [2]. The photocatalytic process is emerging as a promising alternative technology for the oxidation/degradation of VOCs. TiO_2 is superior to other

Email address: andraz.suligoj@ung.si (Andraž Šuligoj)

photocatalysts due to its interesting characteristics: low cost, safety, high stability and high photocatalytic activity. It can therefore promote ambient temperature oxidation of the majority of indoor air pollutants [1]. An important step in the photoreaction is the formation of hole-electron pairs where energy to overcome the band gap between valence band (VB) and conduction band (CB), usually provided by a photon, is required. When the energy provided (by a photon) is equal or larger than the band gap, pairs of electron-holes are created in the semiconductor and the charge transfer will occur between electron-hole pairs and the adsorbed species (reactants) on the semiconductor's surface resulting in the photooxidation. A band gap of 3,2 eV for anatase-TiO_2, requires a light wavelength of 388 nm, which falls within the UV (ultraviolet) range.

Stoichiometric oxidation of toluene leads to the formation of carbon dioxide and water (Eq. 1) and the primary pathway towards complete degradation is believed to be hydrogen abstraction from the methyl group leading to a benzyl radical; three initial routes are proposed for the formation of this radical [3]:

1) direct hole transfer to toluene,
2) H abstraction by an OH radical,
3) H abstraction by a chlorine radical.

$$C_7H_8 + 9\,O_2 \longrightarrow 7\,CO_2 + 4\,H_2O \tag{1}$$

Commercial photocatalytic TiO_2 is already available in the form of powder (e.g. Degussa P25 from Evonik, Hombikat UV100 from Sachtleben Chemie, Millennium PC500 from Cristal Global) or in the form of a colloidal solution (e.g. STS 21 from Ishihara, CCA 100 AS from Cinkarna Celje) with excellent photocatalytic activity. TiO_2 can be used in its powder form, i.e. in slurry and in fluidized bed photoreactors or immobilised on a proper support. Potential methods for coating TiO_2 onto a material are chemical vapour deposition (CVD), electrophoretic deposition, thermal treatment and the sol-gel method [4], from which the latter is the most convenient (inexpensive) and practical [5].

A common approach to enhancing the photocatalytic activity of TiO_2 is increasing its surface area (from 100–200 m^2/g to 400–1000 m^2/g). This can be achieved by immobilizing TiO_2 to a porous SiO_2 support [6–8] or preparing the catalyst in the form of a thin film using an appropriate carrier [9, 10]. It has been suggested that the photocatalytic reaction rate using TiO_2/SiO_2 solid thin films significantly depends on the ratio porosity/surface area together with the interfacial area of the tested compound with the titania layer [9].

Porous silicates with pore sizes ranging from a few nanometers up to several micrometers and with specific surface areas up to 1500 m^2/g have found numerous commercial applications such as adsorbents, molecular sieves, and, particularly, as shape-selective solid catalyst and catalyst supports [11]. The uniform arrangement of pores in porous silicates, their structural and textural diversity, as well as the possibility to modify their chemical (surface) properties, i.e., by functionalisation of the pore surfaces with specific organic ligands, metals or organometallic complexes, offer a wide variety of applications in molecular separations, metal ion trapping, heterogeneous catalysis, etc. [12, 13]. To focus on heterogeneous catalysis, the advantage of using silica (or silicates), due to their hydrophobic surface properties, is an important benefit for oxidation reactions. Typically, hydrophobic reactants, which need to be adsorbed, are converted into hydrophilic products, which need to be expelled from the surface. In addition to designing the pore system, strategies for selective immobilization of TiO_2 nanoparticles inside the channels of mesoporous silicas are crucial for obtaining a well adhered and stable catalyst. Conventional post-synthesis methodologies such as impregnation, ion-exchange, template-ion exchange or direct-synthesis methodologies, such as hydrothermal crystallization, are usually a good choice [14–17]. A Ti : Si molar ratio of 1 :1 turned out to be the optimum one for fast degradation kinetics [8]. Sorolla *et al.* [18] found that inclusion of SBA-15 as a support for copper modified TiO_2 resulted in lower crystalline sizes of catalysts. Ceramics, glass, metals and other materials have mostly been employed for the manufacture of carriers [4].

The objectives of this study were (i) successful low-temperature synthesis of TiO_2/SiO_2 composites with enhanced adsorption and photocatalytic properties, (ii) their immobilisation on sodium glass, (iii) their characterisation and (iv) testing for toluene degradation.

2. Experimental details

2.1. Preparation of the samples

Photocatalytic materials were immobilized on glass plates with dimensions of 24 cm $\times$ 1.2 cm $\times$ 0.2 cm, designed to fit a special Teflon holder in a carberry type photoreactor [19].

2.1.1. Preparation of the mesoporous silica

Disordered mesoporous KIL-2 powders were made in a two-step synthesis [14]. In the first step, tetraethyl orthosilicate (TEOS)[1] and triethanolamine were stirred in solution for 30 min. Then deionized water was added to the mixture, followed by the addition of tetraethylammonium hydroxide (TEAOH). The solution was mixed to obtain a homogeneous gel. The final gel, with a pH of 7 and a molar composition of TEOS : TEA : TEAOH : H_2O = 1 : 0.5 : 0.1 : 11 was aged overnight at room temperature and then dried in an oven for 24 h at 50 °C. In the second step, the gel was solvothermally treated in ethanol in Teflon-lined stainless steel autoclaves at 150 °C for 48 h. Removal of the template was performed by calcination at 500 °C for 10 h using a heating rate of 1 °C/min in air. Using this method, the thermal stability of the product was simultaneously established.

Ordered mesoporous silica SBA-15 powders were synthesized according to the well-known procedure described in [20, 21]. 8 g of Pluronic® P123 triblock copolymer[2] was added to 260 mL of distilled water and 40 mL of concentrated hydrochloric acid (37 wt.%, HCl). The mixture was stirred until the surfactant was dissolved. Next, 17 mL of TEOS were added while stirring at 45 °C. The reaction gel was stirred for 8 h at 45 °C and aged for another 16 h at 80 °C. The obtained gel with molar ratios of reaction components SiO_2 : P123 : HCl : H_2O = 1 : 0.017 : 5.85 : 190 was hydrothermally treated in a stainless steel Teflon-lined autoclave at 100 °C for 24 h. The obtained product was continuously washed with distilled water and dried at room temperature. The surfactant was removed by calcination at 550 °C for 6 h in air flow at a heating rate of 1 °C/min [21].

2.1.2. Preparation of TiO_2/SiO_2 composites

Degussa P25 reference material (denoted as P25) was prepared by dissolving 1.3337 g of Degussa P25 TiO_2 powder[3] in 10 mL of absolute ethanol[4]. PC500 reference material (label PC500) was prepared using the same procedure, only substituting Degussa P25 powder with Millennium PC500 TiO_2 powder[5]. Sample PTN was prepared using a patented procedure [22]. TiO_2 suspensions CCA 100 AS ($\gamma(TiO_2)$ = 239.7 g/L) and CCA

[1] Acros Organics, Geel, Belgium, www.acros.com
[2] BASF, Ludwigshafen, Germany, www.basf.com
[3] Evonik, Essen, Germany, www.evonik.com
[4] Sigma-Aldrich, St. Louis, USA, www.sigmaaldrich.com
[5] Cristal Global, Jeddah, Saudi Arabia, www.cristalglobal.com

100 BS ($\gamma(TiO_2)$ = 368.9 g/L)[6] were deposited in their original form. They were denoted as AS and BS, respectively. Samples CCA 100 AS + SBA-15 (AS/SBA15), CCA 100 BS + SBA-15 (BS/SBA15), CCA 100 AS + KIL-2 (AS/KIL2) and CCA 100 BS + KIL-2 (BS/KIL2) were prepared by mixing titania and silica in a molar ratio [Ti] : [Si] = 1 : 1. 5 mL of 1-propanol[7] were added to the samples and mixed on a magnetic stirrer at 400 rpm for 2 hours. They were then treated in a cold ultrasonic bath for 10 minutes which promotes the infiltration of nanoparticles into the mesopores [23]. SBA-15 blank and KIL-2 blank were prepared by mixing 1.25 mL of double deionized water with 2.5 mL of 1-propanol and adding 0.3200 g of SiO_2 powder. The suspension was then mixed on a magnetic stirrer for 2 hours and sonicated in a cold ultrasonic bath for 10 minutes.

2.2. Deposition of the layers

The glass plates were cleaned using ethanol (96 %) before application of the sol. The photocatalytic sol was deposited to the plates using a brush. Immediately after deposition, the sheets were dried. They were then heat treated in an oven (EUP-K 6/1200)[8] at 150 °C for 1 h. Subsequently, they were washed with ethanol and dried. The procedure of applying the sol and heat treatment was repeated several times until the surface density of 1.0 mg/cm^2 (KERN ABJ 120-4M)[9] was reached.

2.3. Photocatalytic tests

The photoreactor setup is described in detail in [24] (Figure 1), with the only difference being in the GC method where the column (Varian CP-Porabond U, 0.32 mm ID, 25 m) in the GC-MS apparatus (Varian, Saturn 2100T) was set at 80 °C and was heated to 180 °C at a rate of 10 °C/min, where it was held for 2 minutes. Finally, it was cooled down to 80 °C at a rate of 100 °C/min. The injector was set to split mode with a ratio of 10. The mass range in the mass spectrometer was set to 15-50 m/z for the first 3 minutes, for better sensitivity when detecting CO_2, but was then adjusted to 15-150 m/z. The model compound chosen was toluene with an initial concentration of 32 $\pm$ 3 ppmv. The quantification of carbon dioxide was

[6]Cinkarna, Celje, Slovenija, ww.cinkarna.si/en/ultrafinetitaniumdioxide
[7]Carlo Erba, Arese, Italy, www.carloerbareagents.com
[8]Bosio d.o.o., Štore, Slovenia, www.bosio.si
[9]KERN & SOHN GmbH, Balingen, Germany, http://www.kern-sohn.com

carried out by calibration for CO_2 with a 10 L gas bottle, containing 500 ppmv CO_2 in nitrogen[10].

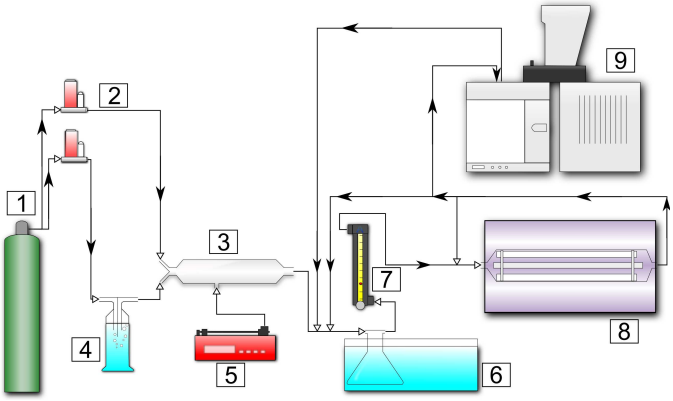

Figure 1: Photoreactor system setup: (1) air cylinder, (2) mass flow controllers, (3) mixing chamber, (4) humidifier, (5) automatic syringe, (6) water bath, (7) flow meter, (8) photoreactor, (9) GC-MS.

2.4. Characterisation

The X-ray powder diffraction (XRD) patterns were obtained on a PANalytical X'Pert PRO high-resolution diffractometer with alpha 1 configuration using $CuK_{\alpha 1}$ radiation (1.5406 Å) in the range from 0.5° to 5° for small-angle range and 5° to 60° for wide-angle range 2 Θ with a step size of 0.033 using a fully opened X'Celerator detector. The peak width at half maximum in the XRD has been used to determine the crystal diameter using the Deby-Scherrer equation:

$$D = \frac{K\lambda}{\beta \cos \Theta} \tag{2}$$

where K(= 0.9) is the Scherrer constant, λ(= 0.15406 nm), the X-ray wavelength, β, the peak width at half maximum, and Θ, the Bragg's diffraction angle. The morphology of samples was studied using a scanning electron microscope Zeiss SupraTM 3VP. Specific surface area was evaluated from adsorption data in the relative pressure range from 0.03 to 0.28 on a Micromeritics Tristar 3000 instrument. Infrared spectroscopy (IR) measurements were made using FT-IR spectrometer Spectrum 100[11]. Spectra were

[10]Messer Austria GmbH, Gumpoldskirchen, Austria, www.messer.at
[11]Perkin Elmer, Massachusetts, USA, www.perkinelmer.com

collected from 450 to 4000 cm^{-1} and processed using Spectrum 6.3.5 software.

3. Results and discussion

3.1. Characterization of the samples

3.1.1. Surface morphology

It is clearly visible from the micro structure that sample AS/SBA15 shows higher porosity and greater structural diversity than sample AS/KIL2. The situation is similar with CCA 100 BS titania, where the differences are even more evident. These samples also exhibit cracks, tens of micrometers long, which indicates bad adherence to the support. However, the hardness tests were not conducted.

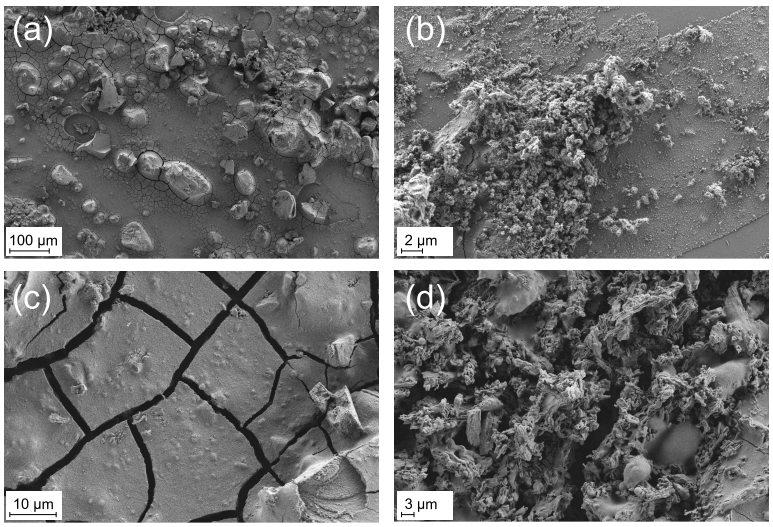

Figure 2: SEM images of (a) AS/KIL2, (b) AS/SBA15, (c) BS/KIL2 and (d) BS/ SBA15.

3.1.2. Crystalline phases

All samples exhibited an anatase crystal structure (Figure 3.1.2), with its characteristic diffraction peaks at 25.3° (101) and 37.8° (004) [25]. Degussa P25 also showed a rutile phase with a peak at 27.4° (110). No other samples apart from the patented composite (which includes P25) exhibited the rutile phase. The smallest crystalline size was observed with sample CCA 100 AS, followed by CCA 100 BS, whereas Degussa P25 exhibited the largest size (Table 1). In the case of CCA 100 AS sample, the crystals became smaller

with the impregnation into mesoporous silica, which is also seen by the broadening of the XRD peaks. This effect is not observed in the CCA 100 BS sample. The reduction in crystalline size was stronger in case of SBA-15 (13.2 to 9.2 nm) than KIL-2 (13.2 to 11.4 nm). This phenomena has been observed before [18] and it is commonly explained by the spacing of pores of SBA-15 or KIL-2, which does not allow the growth of bigger crystals.

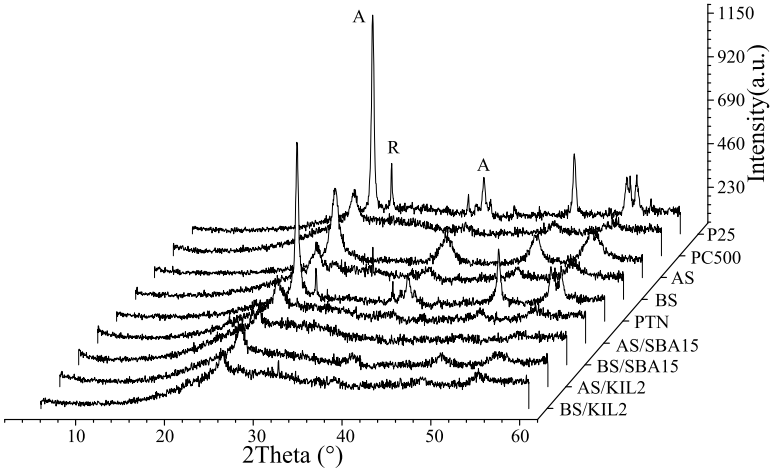

Figure 3: XRD patterns of the samples. The labels A and R correspond to characteristic diffraction peaks of anatase and rutile, respectively.

3.1.3. Chemical composition

The FT-IR spectra of the two TiO_2 suspensions (Figure 4) show the presence of adsorbed water in both samples (blending vibration of H−O−H at 1633 cm^{-1}) as well as O−H and Ti−OH bonds (3438 cm^{-1}). The peak at 1389 is typical from formate species adsorbed onto metallic atoms (Ti−OOCH)[26]. Both samples also consist of TiO_2, as is clear with the existence of Ti−O−Ti bonds (500 cm^{-1}). The sample CCA 100 BS shows additional peaks at 2928 and 2859 cm^{-1} which correspond ν(CH) modes of the methyl group.

3.2. Photocatalytic results

The results of the photocatalytic testing are summarized in Table 1. The CO_2 evolution which also represents the mineralization ratio was calculated using the following equation

$$CO_2(\%) = \frac{[CO_2]_{evolved}}{[CO_2]_{theoretical}} \times 100 \tag{3}$$

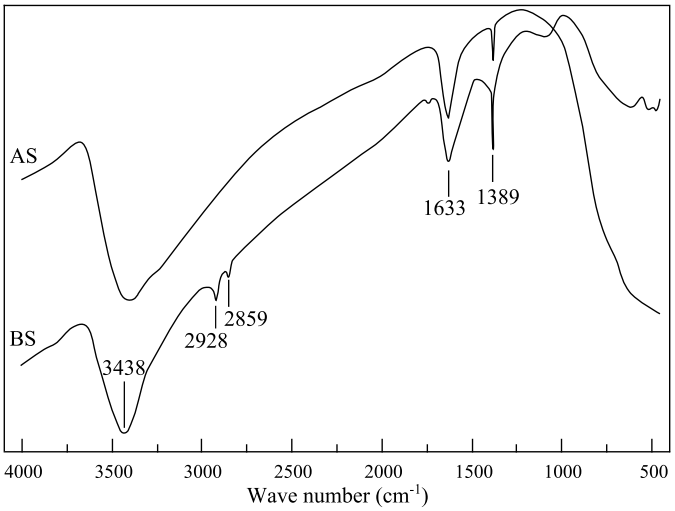

Figure 4: FT-IR spectra of two TiO_2 suspensions.

Where $[CO_2]_{evolved}$ is the final CO_2 concentration detected at the end of the experiment, and $[CO_2]_{theoretical} = 7 \times c_0$, where c_0 is the detected toluene concentration at the beginning of the experiment.

Amongst the raw photocatalytic materials, sample AS showed the best activity with a reaction rate 1.7 times higher than P25 (Table 1). The slowest reaction rate was observed in sample BS which was 1.7 times slower than the P25 reference (Figure 6, 8). In the group of composite materials, the highest photocatalytic activity was observed with sample AS/SBA15 which was 1.3 times faster than AS/KIL2, whereas BS/KIL2 showed the slowest kinetics (7.3 times slower than the fastest composite). The best adsorption capacity showed both SiO_2 blanks; SBA-15 (52.4 %), followed by KIL-2 (51.7 %). AS/SBA15 (26.8 %) and AS/KIL2 (22.7 %) showed more than 3 times higher adsorption than BS/SBA15 (7.23 %) BS/KIL2 (6.61 %). The addition of mesoporous silica improved adsorption capacities significantly (Figure 5), although the increase was higher in the case of SBA-15 (2.8 times for AS/SBA15) than KIL-2 (2.4 times for AS/KIL2). This is easily explained by the increased surface area. Stoichiometric oxidation to CO_2 was observed in samples P25, PC500 and AS/SBA15 with the production of CO_2 being 97.5 %, 97.0 % and 96.8 %, respectively (Table 1, Figure 5). All 3 samples containing CCA 100 BS exceeded the stoichiometric concentration of CO_2 with 218 %, 115 and 114 % of stoichiometric CO_2 produced by BS, BS/SBA15 and BS/KIL2, respectively. Because the oxidation of toluene

was very low in all 3 samples of CCA 100 BS, high CO_2 evolution during the illumination phase could only be produced by oxidation of organic components present in the catalyst itself as proven in Section 3.1.3. The CO_2 evolution in blanks for SBA-15 and KIL-2 could be a consequence of adsorption of organics onto the framework of the silica between the fabrication and testing of the material, as it was stored on ambient air in the dark.

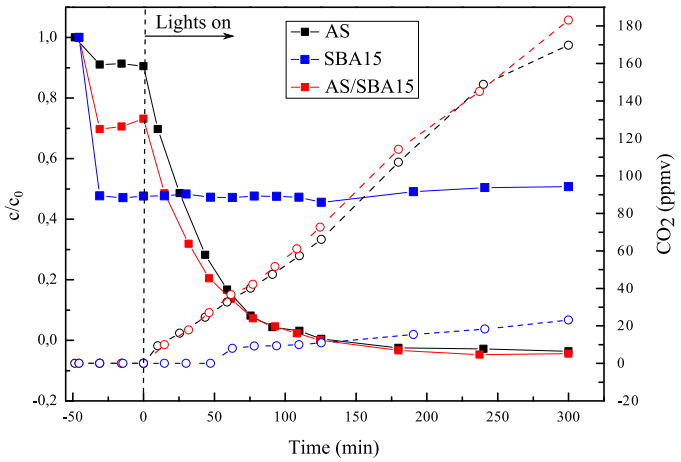

Figure 5: Degradation of toluene ($c_0 = 32$ ppmv) and CO_2 production of three samples. ○, ○ and ○ are the CO_2 productions for sample AS, AS/SBA15 and SBA15 blank, respectively.

High photocatlytic activity of CCA 100 AS could be attributed to its higher surface area, which is 37 % higher than that of CCA 100 BS and more than 6-times higher than that of Degussa P25. Furthermore, the crystal sizes of AS sample are the smallest (Table 1), which indicates that it is likely that CCA 100 AS has better crystallinity. The fact that the CCA 100 BS layer was 2.5-times thicker than the CCA 100 AS layer and 34 % thicker than the P25 layer, could result in higher recombination of the charge carriers, although this leads to better adsorption properties. The photocatalytic performance improved for sample AS where the addition of SBA-15 yielded a 46 % increase in photocatalytic activity. A good correlation between adsorption properties and reaction rate was observed between the composite samples with mesoporous silica added (Figure 7), but not not in other samples including sample PTN in which amorphous silica is present. Its reaction rate is too high compared with other composites, which could be the consequence of its disorganized structure and mixture of two powder titania sources where there is a high chance of a synergistic effect. The

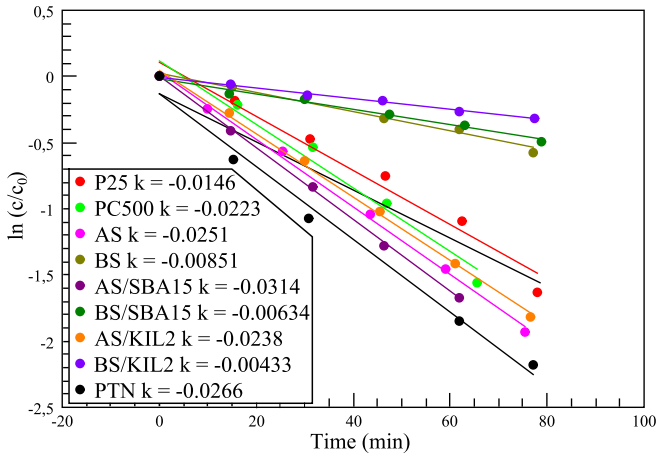

Figure 6: ln (c/c_0) versus time comparison of the samples. Label descriptions are in Table 1.

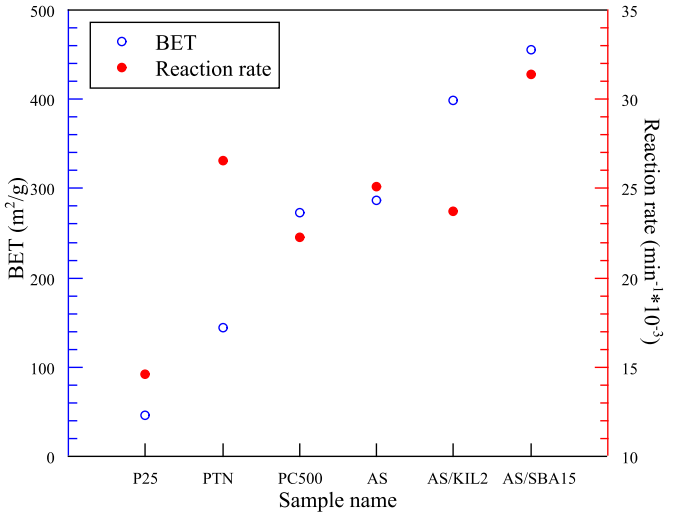

Figure 7: Dependence of reaction rate on surface area.

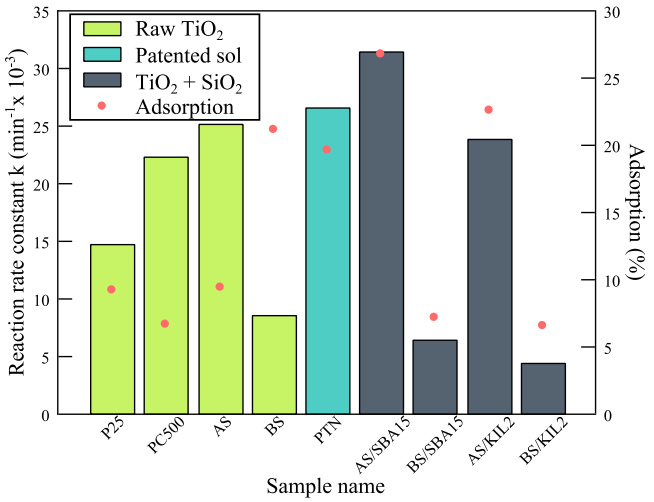

Figure 8: Reaction rate constants and adsorption properties of the samples. ■ are raw TiO_2 materials, ■ samples with mesoporous SiO_2 added, ■ patented sample, ■ sample with the addition of amorphous silica. Label descriptions are in Table 1.

sample AS/KIL2 shows slower reaction kinetics than expected from the surface area. As seen from the SEM images, the surface of the layer seems less open with fewer pores where catalysis can take place.

4. Conclusions

It seems that the ordered structure of SBA-15 plays an important role in photocatalytic properties of materials immobilized into its pores. The differences are present in the crystal sizes of titania trapped in the pore mesh as well as in adsorption and especially in photocatalytic activity. The pores of the silica support have a strong influence on photocatalyst's crystal size, mainly due to trapping the crystals inside the pores. A good correlation between surface area and reaction rate was found for most catalysts and composites fabricated, which indicates the importance of this factor. However, it is important to remember that this is not the only property which influences the final activity of the material.

5. Acknowledgments

The authors of this paper would like to thank the Slovenian research agency for financially supporting this work. They would also like to thank

Table 1: Structural and photocatalytic properties of the photocatalytic thin layers.

Sample	Ads. (%)	k (min^{-1})	CO_2 (%)	S_{BET} (m^2/g)	d (μm)	Crystal size (nm)
P25	9.26	0.0146	97.5	46,4	8.5	22.6–37.5
PC500	6.74	0.0223	96.8	273	/	9.20–12.8
AS	9.50	0.0251	65.8	287	4.5	7.80–13.2
BS	21.2	0.00851	218	209	11.4	9.20–10.3
PTN	19.7	0.0266	69.8	144	4.8	21.2–35.1
AS/SBA15	26.8	0.0314	97.0	455	24.2	8.60–9.20
BS/SBA15	7.23	0.00634	115	367	13.6	10.3
AS/KIL2	22.7	0.0238	75.9	398	5.0	11.4
BS/KIL2	6.61	0.00433	114	327	5.1	12.8
AS 7C	13.3	0.0360	92.8	132	5.9	7.80–11.3
BS 7C	11.8	0.00369	73.3	213	3.3	7.80–19.0
AS 7C/SBA	28.9	0.0333	93.1			
SBA-15	52.4	0.0	8.67			
KIL-2	51.7	0.0	7.48			

Cinkarna Celje for providing material and financial support.

[1] S. Wang, H. M. Ang, and M.O. Tade. Volatile organic compounds in indoor environment and photocatalytic oxidation: State of the art. *Environment international*, 33(5):694–705, 2007.

[2] M. Hodgson, H. Levin, and P. Wolkoff. Volatile organic compounds and indoor air. *Journal of Allergy and Clinical Immunology*, 94:296–303, 1994.

[3] O. d'Hennezel, P. Pichat, and D. F. Ollis. Benzene and toluene gas-phase photocatalytic degradation over H_2O and HCl pretreated TiO_2: by-products and mechanisms. *Journal of Photochemistry and Photobiology A: Chemistry*, 118(3):197–204, 1998.

[4] A. Y. Shan, T. I. M. Ghazi, and S. A. Rashid. Immobilisation of titanium dioxide onto supporting materials in heterogeneous photocatalysis: A review. *Applied Catalysis A: General*, 389(1–2):1–8, 2010.

[5] U. Černigoj, U. L. Štangar, P. Trebše, U. O. Krašovec, and S. Gross. Photocatalytically active TiO_2 thin films produced by surfactant-assisted sol-gel processing. *Thin Solid Films*, 495(1–2):327–332, 2006. EMRS

2005 Symposium E: Synthesis, Characterization and Applications of Mesostructured Thin Layers.

[6] S. Rodrigues, K. T. Ranjit, S. Uma, I. N. Martyanov, and K. J. Klabunde. Single-step synthesis of a highly active visible-light photocatalyst for oxidation of a common indoor air pollutant: Acetaldehyde. *Advanced Materials*, 17(20):2467–2471, 2005.

[7] M. Tasbihi, U. L. Štangar, A. S. Škapin, A. Ristič, V. Kaučič, and N. N. Tušar. Titania-containing mesoporous silica powders: Structural properties and photocatalytic activity towards isopropanol degradation. *Journal of Photochemistry and Photobiology A: Chemistry*, 216(2–3):167–178, 2010. 3rd International Conference on Semiconductor Photochemistry, SP-3, April, 2010, Glasgow UK.

[8] M. Tasbihi, U. L. Štangar, U. Černigoj, J. Jirkovsky, S. Bakardjieva, and N. N. Tušar. Photocatalytic oxidation of gaseous toluene on titania/mesoporous silica powders in a fluidized-bed reactor. *Catalysis Today*, 161(1):181–188, 2011. Selected contributions of the 6th European Meeting on Solar Chemistry and Photocatalysis: Environmental Applications (SPEA 6), 13th to 16th June 2010.

[9] U. Černigoj, M. Kete, and U. L. Štangar. Development of a fluorescence-based method for evaluation of self-cleaning properties of photocatalytic layers. *Catalysis Today*, 151(1–2):46–52, 2010. 2nd European Conference on Environmental Applications of Advanced Oxidation Processes(EAAOP-2).

[10] J. Taranto, D. Frochot, and P. Pichat. Photocatalytic air purification: Comparative efficacy and pressure drop of a TiO_2-coated thin mesh and a honeycomb monolith at high air velocities using a 0.4 m^3 close-loop reactor. *Separation and Purification Technology*, 67(2):187–193, 2009.

[11] J. Sun and X. Bao. Textural manipulation of mesoporous materials for hosting of metallic nanocatalysts. *Chemistry-A European Journal*, 14(25):7478–7488, 2008.

[12] A. Taguchi and F. Schüth. Ordered mesoporous materials in catalysis. *Microporous and mesoporous materials*, 77(1):1–45, 2005.

[13] J. C. Jansen, Z. Shan, L. Marchese, W. Zhou, N. vd Puil, and T. Maschmeyer. A new templating method for three-dimensional mesopore networks. *Chemical Communications*, 8(8):713–714, 2001.

[14] N. N. Tušar, A. Ristić, G. Mali, M. Mazaj, I. Arčon, D. Arčon, V. Kaučič, and N. Z. Logar. Mnox nanoparticles supported on a new mesostructured silicate with textural porosity. *Chemistry - A European Journal*, 16(19):5783–5793, 2010.

[15] N. N. Tušar, N. Z. Logar, I. Arčon, G. Mali, M. Mazaj, A. Ristič, K. Lazar, and V. Kaučič. Local environment of iron in the mesoporous hexagonal aluminophosphate catalyst. *Microporous and Mesoporous Materials*, 87(1):52–58, 2005.

[16] M. Mrak, N. N. Tušar, N. Z. Logar, G. Mali, A. Kljajić, I. Arčon, F. Launay, A. Gedeon, and V. Kaučič. Titanium containing microporous/mesoporous composite (Ti,Al)-Beta/MCM-41: Synthesis and characterization. *Microporous and Mesoporous Materials*, 95(1–3):76–85, 2006.

[17] M. Mazaj, S. Costacurta, N. Zabukovec Logar, G. Mali, N. Novak Tušar, P. Innocenzi, L. Malfatti, F. Thibault-Starzyk, H. Amenitsch, V. Kaučič, and G. J. A. A. Soler-Illia. Mesoporous aluminophosphate thin films with cubic pore arrangement. *Langmuir*, 24(12):6220–6225, 2008. PMID: 18479152.

[18] M. G. Sorolla II, M. L. Dalida, P. Khemthong, and N. Grisdanurak. Photocatalytic degradation of paraquat using nano-sized Cu-TiO_2/SBA-15 under UV and visible light. *Journal of Environmental Sciences*, 24(6):1125–1132, 2012.

[19] U. Černigoj, U. L. Štangar, and P. Trebše. Evaluation of a novel Carberry type photoreactor for the degradation of organic pollutants in water. *Journal of Photochemistry and Photobiology A: Chemistry*, 188(2–3):169–176, 2007.

[20] D. Zhao, J. Feng, Q. Huo, N. Melosh, G. H. Fredrickson, B. F. Chmelka, and G. D. Stucky. Triblock copolymer syntheses of mesoporous silica with periodic 50 to 300 angstrom pores. *Science*, 279(5350):548–552, 1998.

[21] M. Mazaj, W. J. Stevens, N. Z. Logar, A. Ristič, N. N. Tušar, I. Arčon, N. Daneu, V. Meynen, P. Cool, E. F. Vansant, and V. Kaučič. Synthesis and structural investigations on aluminium-free Ti-Beta/SBA-15 composite. *Microporous and Mesoporous Materials*, 117(1–2):458–465, 2009.

[22] A. Šuligoj, U. Černigoj, and U. L. Štangar. Preparation procedure of durable titania coatings on metal supports for photocatalytic cleaning applications, 2010. P-201000432 (Ljubljana: Urad Republike Slovenije za intelektualno lastnino).

[23] N. V. Dezhkunov and T. G. Leighton. Study into correlation between ultrasonic capillary effect and sonoluminescence. *Journal of Engineering Physics and Thermophysics*, 77(1):53–61, 2004.

[24] M. Tasbihi, M. Kete, A. Raichur, N. N. Tušar, and U. L. Štangar. Photocatalytic degradation of gaseous toluene by using immobilized titania/silica on aluminum sheets. *Environmental Science and Pollution Research*, 19:3735–3742, 2012.

[25] H. D. Nam, B. H. Lee, S. J. Kim, C. H. Jung, J. H. Lee, and S. Park. Preparation of ultrafine crystalline TiO_2 powders from aqueous $TiCl_4$ solution by precipitation. *Japanese Journal of Applied Physics*, 37(Part 1, No. 8):4603–4608, 1998.

[26] J. Araña, O. González Díaz, M. Miranda Saracho, J. M. Doña Rodríguez, J. A. Herrera Melián, and J. Pérez Peña. Photocatalytic degradation of formic acid using Fe/TiO_2 catalysts: the role of Fe^{3+}/Fe^{2+} ions in the degradation mechanism. *Applied Catalysis B: Environmental*, 32(1–2):49–61, 2001.

Characterization of Photocatalytic Layers Containing Titanium-Dioxide Nanoparticles

Marko Kete[a]

[a]*Laboratory for Environmental Research, University of Nova Gorica, Vipavska 13, 5001 Nova Gorica, Slovenia*

Abstract

Photocatalytic properties of titanium(IV) oxide (TiO_2) in anatase form can be used for various purposes, including photocatalytic purification of water. For such an application suspended or fixed photocatalytic reactors are used. Those with fixed phase seem to be preferred due some characteristics, one of them is no need for photocatalyst filtration. Due problems with leaching and peeling off of the fixed phase, immobilization procedure and good adhesion is crucial. Within the present work, we present physical and photocatalytic characterization results of five commercially available TiO_2 photocatalysts (P25, P90, PC500, KRONOClean 7000, VPC-10), one pigment (Hombitan LO-CR-S-M) and two mixtures (P25+PC500, P25+KRONOClean 7000), which were successfully immobilized on glass slides by sol suspension procedure. Photocatalytic tests were carried out under UVA and UV-Vis irradiation, using a method based on the detection of the fluorescent oxidation product of terephthalic acid (TPA), ie. hydroxy terephthalic acid (HTPA). Simple and fast detection was done using microplate reader. Aeroxide® P90 incorporated in to the binder was the most photocatalytically active layer and, unlike the others showed linear photocatalytic activity through the entire range of tested UVA irradiation intensities (2.3 mW/cm^2 - 6.4 mW/cm^2).

Keywords: photocatalytic layers, titanium dioxide nanoparticles, hydroxy terephthalic acid

1. Introduction

Due to its photocatalytic properties, TiO_2 in anatase or anatase/rutile crystalline structure has three major potential areas of application: (I) production of self-cleaning surfaces based on photoinduced superhydrophilicity [1], (II) degradation of volatile organic/inorganic compounds from gas phase [2–4] and (III)

Email address: marko.kete@ung.si (Marko Kete)

waste water treatment [5, 6] or pretreatment and disinfection [7–9] of drinking water. Photocatalytic reactors used for water treatment can be classified according to either those with an immobilized photocatalyst, such as the different forms of fixed bed reactors, or reactors with suspended photocatalyst in the aqueous media, the so-called slurry reactors. Photocatalytic reactors with TiO_2 immobilized on the surface of an inert support may be further divided in to four principal types: (I) membrane, monoliths, or equivalent forms of catalytic wall reactors, (II) optical fiber reactors, (III) fluidized bed reactors, and (IV) packed bed reactors [10]. Among the mentioned reactor types, packed-bed and monolith photocatalytic reactors offer several important advantages: (I) in contrast to slurry reactors, no post-separation process is needed, (II) the photocatalytic surface could be significantly increased by using the proper substrate (glass beeds, fibres, foamed ceramics), (III) these substrates or fillers enhance the mixing of reactants, which tends to reduce undesirable diffusive resistances, and finally, (IV) these two types of photocatalytic reactors have less catalysts attrition problems then the ones present in fluidized bed reactors. In all cases, the immobilization procedure is crucial, which means that at least the following three conditions should be satisfied: good adhesion, which enables layer durability without photocatalyst leaching and peeling off, non-deactivation of the photocatalyst by the attachment process and high specific surface area [10–12]. There are many different methods for the immobilization of TiO_2 photocatalyst. A promising alternative strategy for producing a highly active photocatalytic coating is the attachment of stable photocatalyst particles onto a support without any reduction in activity. Numerous techniques were reported for preparing supported titania, for instance, sol–gel, chemical vapour deposition, electrodeposition, sol-spray, hydrothermal, hybrid immobilisation procedure [12] and an all-titania washcoating method [13]. In addition to these, effective immobilization could also be achieved by a novel low temperature hybrid sol-suspension method [14]. This procedure has several advantages, easy replication of the method, a simple procedure and potentially easy application to various substrates (aluminium, glass, glass fibres, quartz wool, Al_2O_3 monoliths). As will be shown in the following paper, the hybrid sol-suspension method can be used to prepare stable, moderately thick and highly active photocatalytic layers with almost any commercial TiO_2 nanoparticles.

Photocatalytic activity of the prepared photocatalytic layers was determined under different light intensities using a sensitive method based on the detection of fluorescent hydroxy terephthalic acid (HTPA), which is produced during the photodegradation process of terephthalic acid (TPA) [15]. In the past the method has been developed in the past for the purpose of determining self-cleaning photocatalytic properties of layers and as a possible alternative method for contact angle (CA) measurements (ISO 27448: 2009). CA method suffers from the slow oxidation (degradation) process of a solid fatty deposit, it is indirect and therefore

less reliable with variable repeatability [16]. Within the present work certain improvements of the fluorescent method will be presented, which enable the rapid and accurate detection of HTPA.

2. Experimental details

2.1. Chemicals used

The following chemicals were used as purchased: terepthalic acid (TPA) from Alfa Aesar, NaOH from Sigma-Aldrich, hydroxyethyl-cellulose (HEC), titanium(IV) tetraisopropoxide (TTIP) from Fluka, tetraethoxysilane from J.T. Baker, Levasil 200/30% colloidal SiO_2 from H.C. Starck, absolute ethanol from Sigma-Aldrich, 96% ethanol from Itrij. All aqueous solutions were prepared using highly pure water from the NANOpure system (Barnstead). Commercial TiO_2 nanopowders were obtained from: Evonik Degussa (Aeroxide® P25 and P90), Cristal Global (Milleniumm/CristalACTiV™ PC500), Kronos (KRONOClean 7000), Tipe (VPC-10), Sachtleben Chemie GmbH (Hombitan LO-CR-S-M).

2.2. Sol suspension preparation and deposition

The sol suspensions of commercial nano TiO_2 were prepared according to the preparation procedure described in the national patent application [14]. Titanium isopropoxide (TTIP) in ethanolic solution was hydrolyzed by acidic ($HClO_4$) aqueous solution. During uncontrolled hydrolysis and condensation reaction of TTIP, a white precipitate of hydrated amorphous TiO_2 was formed, which was then refluxed for 48 h, causing the crystallization and disaggregation of TiO_2, resulting in stable nanocrystalline titania sol. Separately, a homogeneous silica sol was prepared from TEOS, deionized water and HCl. The nanocrystalline titania sol, the silica sol, colloidal SiO_2 and ethanol were gradually mixed together to give a binder sol. Finally, commercial nanopowder or mixture of two nanopowders was suspended in the binder sol. The titania/binder sol was then placed in a cold ultrasonic bath for 10 min to obtain the final sol suspension containing 6.8 wt.% TiO_2. Photocatalytic layers were preprared by dip-coating using a homemade dip-coating device with a pulling speed of 10 cmmin^{-1}. After application, the layer was dried using hairdryer and placed in to a furnace [1] at 150 °C for 1h. Dipcoating-heating cycle was repeated util the required specific surface mass was obtained (0.55 – 0.77 mg cm^{-2}).

[1] EUP-K 6/1200 Laboratory furnace, Bosio d.o.o., Slovenia

2.3. Characterization of thin layers

2.3.1. Determination of physical properties

The thickness of photocatalytic layers was determined using a Taylor–Hobson Talysurf profilometer. Absorbance and difuse reflectance were measured on pure titania layers using UV/Vis spectrophotometer with integrating sphere [2]. Band gap energies were determined by plotting the Kubelka–Munk transformation of the original difuse reflectance coordinates spectra vs. photon energy (hν). The specific surface area was determined according Brunauer–Emmett–Teller (BET) theory, using nitrogen sorption isotherms obtained at 77.3 K [3]. Before measurements of BET surface, samples were cleaned and dried during flushing with nitrogen (5.0) for 4 to 6 h at 130 °C. Thin film topography was investigated with an atomic force microscop (AFM) Veeco CP-II instrument [4], operating in non-contact mode in atmospheric conditions. The probe tip radius was approximately 10 nm. The micrographs of different samples were acquired approximately at the same position in the center of the layer, consequently avoiding any possible border effects. The one-dimensional autocorrelation function was calculated along the fast scanning axis and averaged over slow scanning axis. The autocorrelation function was modeled with the Gaussian function

$$G(x) = \sigma e^{\left(\frac{-x^2}{T^2}\right)} \tag{1}$$

where σ denotes root mean square deviation of the heights and T is the autocorrelation length. The X-ray powder diffraction (XRD) patterns were obtained on a X-ray diffractometer [5] using CuKα1 radiation (1.5406 Å) with a step size of 0.017° 2θ and a fully opened X'Celerator detector. The diffractograms were collected in continuous mode in the range of 5.01–89.98° 2θ while rotating the sample. The average crystallite sizes were determined from Scherrer's equation using the broadening of the anatase diffraction peaks.

XRD and nitrogen sorption characterization were performed on "film powder" samples, which were obtained by carefully scratching a number of coatings and collecting the powder.

2.4. Photocatalytic activity - degradation of TPA layer and HTPA detection

Photocatalytic tests were carried out in the UVA photochamber reactor and sun simulator [6] chamber with simulated solar irradiation source (300 – 800 nm).

[2] LAMBDA 650 UV/Vis with 150 mm integrating sphere, Perkin Elmer, USA (http://www.perkinelmer.com/)

[3] Tristar II 3020 Surface Area Analyzer, Micromeritics, USA (http://www.micromeritics.com/)

[4] Model NSC15-AlBS, MikroMasch, USA (http://www.mikromasch.com/)

[5] X′Pert PRO MPD, PANalytical, Netherlands (http://www.panalytical.com)

[6] Suntest XLS+, Atlas, USA (http://atlas-mts.com/)

Each type of film was tested at three different irradiation conditions: (I) in a photochamber at 2.31 $mWcm^{-2}$ (300 – 400 nm), (II) Suntest XLS+ at 287 Wm^{-2} (300 – 800 nm) containing 2.97 $mWcm^{-2}$ of UVA (300 – 400 nm), (III) Suntest XLS+ at 450 Wm^{-2} (300 – 800 nm) containing 4.17 $mWcm^{-2}$ of UVA (300 – 400 nm) and (IV) Suntest XLS+ at 750 Wm^{-2} (300 – 800 nm) containing 6.39 $mWcm^{-2}$ of UVA (300 – 400 nm). The radiation flux in the photochamber and Suntest XLS+ was measured using an UV detector (300 – 400 nm) [7].

The pure titania layers were first pre-irradiated in the UVA photochamber reactor for 2 h and then tested using a novel highly sensitive fluorescence-based method [15], which is based on the deposition of a thin transparent solid layer of terepthalic acid (TPA) over a photocatalytically active titania layer. After irradiation of the layer system using UVA light, along with other degradation products a highly fluorescent hydroxyterephthalic acid is also formed due to a reaction between the photoexcited TiO_2 and terephthalic acid, which can be detected by various analytical methods (HPLC-FLD, spectrofluorimeter).

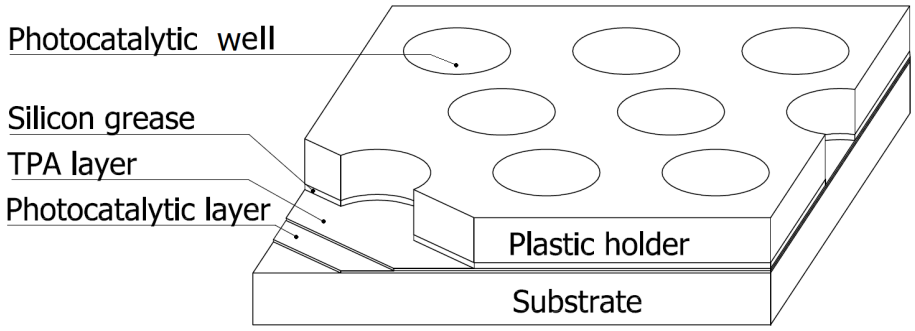

Figure 1: Plastic holder for creating "wells" (10-14) with photocatalytic bottom. Hole diameter ϕ = 9 mm.

To make the analytical procedure rapid, we use a special plastic holder (Figure 1) with holes (ϕ = 9 mm), which was attached to the layer system using silicon grease. The purpose of such a holder was to create "wells" with a photocatalytic bottom. That allowed us to analyze a sample multiple times under different conditions from the same sample. Samples were obtained by washing the "wells" with an automatic pipette using an ethanol/water mixture. Each sample obtained by washing (159 μL $\rightarrow$ 0.25 $mLcm^{-2}$) was then put separately in microplate well [8] and immediately after that fluorescence measurements using microplate reader

[7] XenoCal BB 300–400 UV detector, Atlas, USA (http://atlas-mts.com/)

[8] Microplate with 96 wells (flat bottom, black), Greiner Bio-One, Germany (http://www.greinerbioone.com)

[9] were performed. The wavelength of exitation was 320 nm (filter bandwidth: 25 nm) and emission was measured at 430 nm (filter bandwidth: 35 nm). The instrument was operating in top mode with 25 reads per well, with 20 μs integration time. The amplification factor for the photomultiplier tube was 56 or 78, respectively. Obtained results were than recalculated to corresponding concentrations using calibration curves, plotted and fit according to a simplified kinetic analysis (Figure 2). In case of each photocatalytic layer, two paralel photocatalytic tests were done to calculate average and standard deviation.

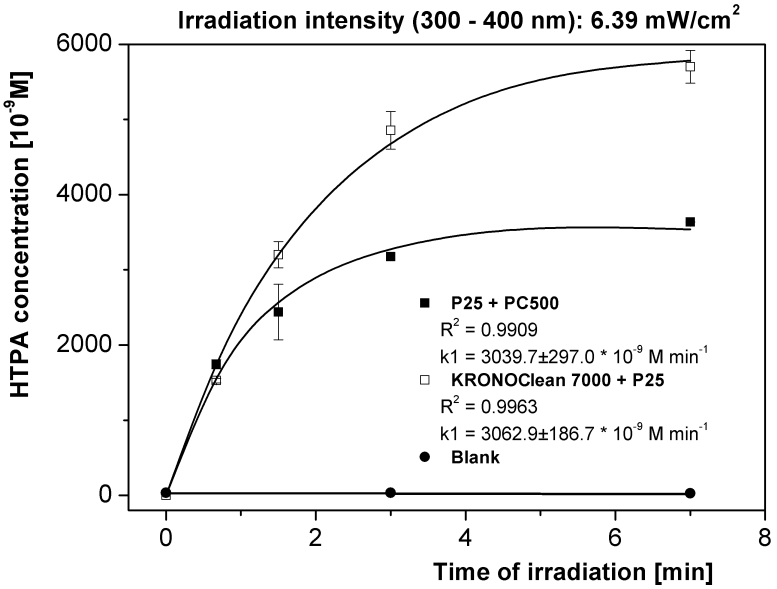

Figure 2: HTPA formation during TPA photocatalytic degradation. In first minutes the concentration of HTPA rapidly increases (k_1). Due lack of TPA and HTPA degradation (k_2), the concentration reaches a plateau and eventually starts to decrease.

A fitting of the data according to a simplified kinetic analysis has been performed for the initial formation of HTPA (until reaching the plateau). The fitting function [15] can be represented by the equation:

$$c_{[HTPA]} = \frac{k_1}{k_2}\left(1 - e^{-k_2 \cdot t}\right), \tag{2}$$

where $c_{[HTPA]}$ represents molar cocentration of the HTPA. According to the

[9] Infinite F200 Microplate reader, Tecan, Switzerland (http://www.tecan.com/)

fitted data (Figure 2) the HTPA formation follows zero-order kinetics (formation rate constant = k_1). This data was then used for determination of photocatalytic activity of photocatalytic layers.

3. Results and discussion

3.1. Physical and chemical properties

Structural investigations give some interesting data regarding the prepared photocatalytic layers and "film powder" samples (Table 1). Despite the approximately same photocatalyst loading (0.65 ± 0.10 mg cm^{-2}), thicknesses of the layers varied significantly (1.9 – 5.5 μm). The reason for this could be the particle size of photocatalysts, which seems to be in good correlation with the thickness, so that smaller particles form thinner layers. The exception was Hombitan LO-CR-S-M where there was no increase in layer thickness. However, according to Krysa *et al.* [17] and our experience, a layer thickness between 1 to 1.5 μm is thick enough to absorb more than 90% of UVA (355 nm) radiation. They show that there was no increase of oxalic acid degradation rate when thickness of photocatalytic layer was above 1.0 μm. We therfore believe, that prepared photocatalytic layers can be compared in their photocatalytic performance since they are thicker then $>$ 1.9 μm.

Table 1: Physical characteristics of photocatalytic layers and BET surface areas for "film powder" samples.

Photocatalytic layer	Specific surface mass [mg/cm^2]	Thickness [μm]	Particle size [nm]	Indirect Band gap [eV]	BET surface [m^2/g]
P25	0.68 ± 0.03	4.5	18 - 45	3.02	96.1
P90	0.76 ± 0.02	3.2	13 - 24	3.03	130.2
PC500	0.57 ± 0.06	1.9	6 - 15	3.24	240.5
Hombitan LO-CR-S-M	0.55 ± 0.02	3.4	61 - 100	3.07	56.1
VPC-10	0.61 ± 0.04	3.7	9 - 21	3.15	85.2
KRONOClean 7000	0.77 ± 0.05	5.5	11 - 14	3.21	220.3
PC500 + P25	0.61 ± 0.03	3.5	10 - 40	3.11	172.5
KRONOClean 7000 + P25	0.68 ± 0.02	4.1	13 - 38	3.14	168.8

The BET surfaces of "film powder" samples were higher or lower in comparison to BET surfaces of pure photocatalysts (Table 2), which is due to the silica binder, which is due to the silica binder. It was observed that binder increases the porosity of the pure photocatalyst, when it's BET surface is $<$ 100 m^{2}g^{-1} (P25, P90), but on the other hand to a lesser extent decreases it when BET surface of pure photocatalyst is higher ($>$ 200 m^{2}g^{-1} $\rightarrow$ PC500).

Table 2: BET surface areas of some photocatalysts nanoparticles and their corresponding layers.

Photocatalyst	BET surface [m^2/g]	BET surface of "film powder" samples [m^2/g]
P25	52.4	96.1
P90	99.5	130.2
PC500	286.3	240.5

The surface roughnesses investigated by AFM are presented in terms of root mean square deviation (RMS) of heights on a 2 μm x 2 μm area in Table 3. We note that the roughness is between 23 nm and 150 nm and it is not in correlation to particle size. Since the dip-coating technique, which was used for layer application, is dependent on various parameters, such as viscosity of sol suspension, temperature and humidity, it is very difficult to control the process to such an extent as to produce layers with the same roughness (Figure 3). However, the prepared photocatalytic layers had comparable Surface/Projected surface ratios and we did not detect any effect ot the roughness on photocatalytic performance.

Table 3: Roughness and surface areas of photocatalytic layers obtained by AFM investigations.

Photocatalytic layer	Projected surface [$\mu m \times \mu m$]	Rms [nm]	Surface area [μm^2]	Surface/Projected surface ratio
P25	2×2	44.40	4.97	1.24
P90	2×2	23.20	4.80	1.20
PC500	2×2	87.10	4.60	1.15
Hombitan LO-CR-S-M	2×2	121.50	5.84	1.46
VPC-10	2×2	70.00	4.52	1.13
KRONOClean 7000	2×2	151.80	6.58	1.65
PC500 + P25	2×2	96.10	4.75	1.19
KRONOclean 7000 + P25	2×2	76.20	5.06	1.27

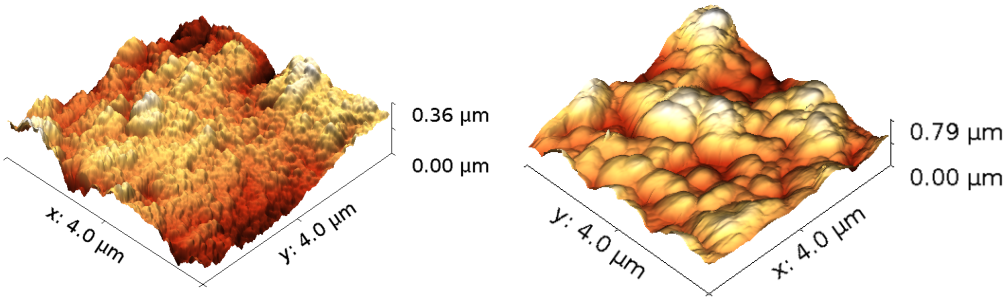

(a) P90

(b) Hombitan LO-CR-S-M

Figure 3: 4×4 μm 3D topography scan of (a) P90, most active photocatalyst and (b) Hombitan LO-CR-S-M, photocatalyst with lowest photocatalytic activity of all tested samples obtained by AFM. One can see that P90 layer has finer surface structure and lower roughness than Hombitan LO-CR-S-M.

Using XRD analysis (Figure 4) of "film powder" samples, we proved that samples PC500, KRONOClean 7000 and VPC-10 are single-phase (anatase) photocatalysts, while Hombitan LO-CR-S-M, P25 and P90 additionally contain rutile in proportions 26 %, 13 % and 18 %, respectively. The ratio of both phases in case of P25 is slightly different as in the case of Ohtani *et al.* [18], due to the fact that in our case amorphous phase was not considered. According to data obtained from producers, there are different proportions of amorphus phase (0 % - 12 %), where KRONOClean 7000 contains the highest proportion. According to particle size, pure photocatalyst samples could be divided in to three groups: (I) >40 nm (Hombitan LO-CR-S-M), (II) 20 – 40 nm (P25) and (III) <20 nm (P90, PC500, KRONOClean 7000 and VPC-10). Both mixed samples were in the range 10 - 40 nm, due to the fact that we used Aeroxide® P25 and two photocatalysts with a particle size of <20 nm (Table 1).

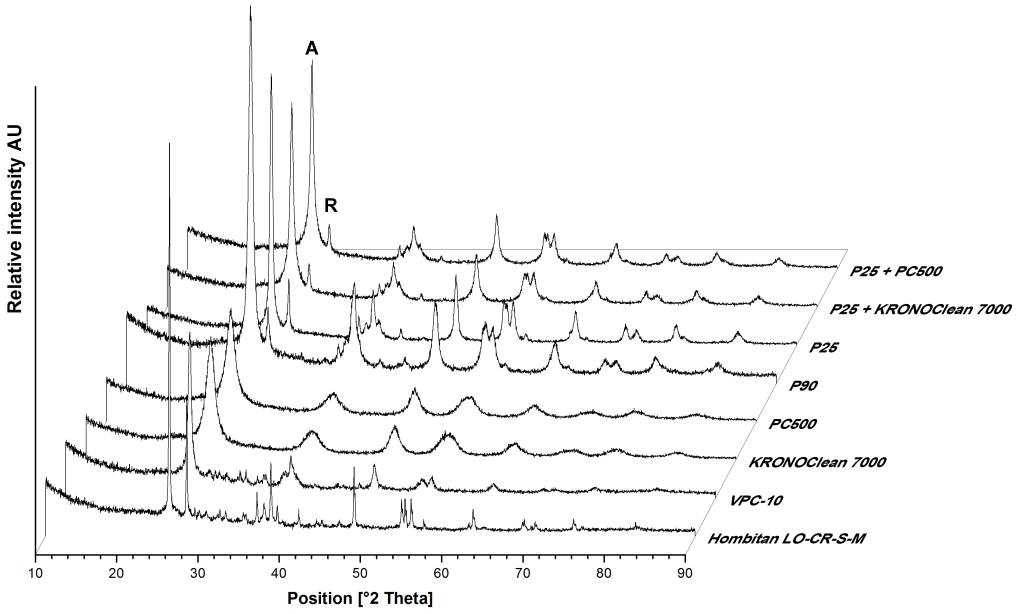

Figure 4: Results of all eight "film powder" samples obtained by XRD analysis. Samples can be clearly distinguished by their crystalline structure to those with pure anatase phase and mixed anatase/rutile phase. This distinction can be made using the first characteristic peaks of both crystalline structures: (I) anatase-A at 2θ = 25.07 ° and (II) rutile-R at 2θ = 27.45 °.

Band gap calculations reveal that both Aeroxide® P25 and P90 photocatalysts have the lowest bandgap energy (3.02 - 3.03 eV $\rightarrow$ 410 nm) which probably has its origins in the phase composition [19]. On the other hand doped photocatalysts need photoactivation photons with higher energies. The UV-Vis difuse reflectance measurements show some decrease under 480 nm (VPC-10) and 550 nm (KRONOClean 7000 and P25 + KRONOClean 7000), but this doesn't result in a lower bandgap. Ohtani [20] highlighted two major problems regarding doping of photocatalyst: (I) in many cases photocatalyst has a modified surface, so it is not actually doped and (II) estimation of band-gap energy, especially for doped samples is very difficult due to the influence of impurities or surface electronic states on absorption spectra. Both phenomena seem to appear in case of doped pure and mixed photocatalysts, since there is no effect on narrowing of bandgap energy (Table 1) or increase of photocatalytic activity (Figure 5). In addition to this, Almquist and Biswas [21] investigated the effect of TiO_2 particle size on its photocatalytic activity and concluded that the optimum nanoparticle size is between 20 - 30 nm due to the strong dependence of light absorption and scattering

efficiencies and charge carrier dynamics at particle sizes of less than 30 nm. They show that significant size quantization effects takes place for anatase nanoparticles below 10 nm. Similarly Lin *et al.* [22] confirmed an increase in band gap energy for particles <10 nm which is in good correlation with our bandgap measurements. On the other hand, we proved that BET surface and crystallinity have a greater influence on photocatalytic activity.

3.1.1. Photocatalytic activity evaluation

Results of hydroxyterephthalic acid (HTPA) formation constants under different irradiation conditions (Figure 5) show that highest HTPA formation rate constants of prepared photocatalytic layers were acheved at different photon fluxes. While for most photocatalysts, this limit is achieved at a moderately low photon flux (3.0 mW/cm^2), which is similar to Brosillon *et al.* [23] obtained in liquid phase, KRONOClean 7000 and to a lesser extent KRONOClean 7000+P25 photocatalytic mixture needed higher irradiation intensity, which is approximately double in value (6.4 mW/cm^2). Remarkable results were obtained using P90 photocatalytic layer, which reveal completely different behavior and a linear increase in HTPA degradation even at high irradiation intenisties. Overall, photocatalytic activity evaluation experiments revealed that P90 incorporated in to the binder indicates the highest activity under all tested irradiation intensities (2.3 mW/cm^2 - 6.4 mW/cm^2) of all tested photocatalytic layers.

Photocatalytic activity of P25 and PC500 mixture was slightly higher in comparison to pure PC500 photocatalyst and one can conclude that synergistic effects could be the reason. The difference in photocatalytic activity is, however within the standard deviation and more repetitions would be required to confirm the existence of synergistic effects. Similar observations could be detected by the photocatalytic activity of P25+KRONOClean 7000 mixture where at different light intensities each of the used photocatalyst plays its role of "leading" photocatalyst, but finally in the end do not lead to synergistic effects. From the results of KRONOClean 7000 photocatalyst, one can see a significant increase of photocatalytic activity when a test was done under sunlight simulation (287 Wm^{-2} $\rightarrow$ 3.0 mW/cm^2 of UVA). This difference could be the evidence for visible light-induced photocatalysis, but to confirm this further photocatalytic tests should be done. On the other hand, VPC-10 didn't indicate such an effect and here we can conclude that doping does not contribute to better photocatalytic activity. The photocatalyst with the lowest activity was Hombitan LO-CR-S-M, which is not actually meant to be used as a photocatalyst but rather as a weather resistant pigment additive. Plotting HOTPA formation constants against BET surface (Figure 6) revealed good correlation between photocatalytic activity and the surface of the photocatalyst. One could draw different curves through the data and notice that BET surface $>$ 170 m^{2}g^{-1} does not contribute significantly to higher pho-

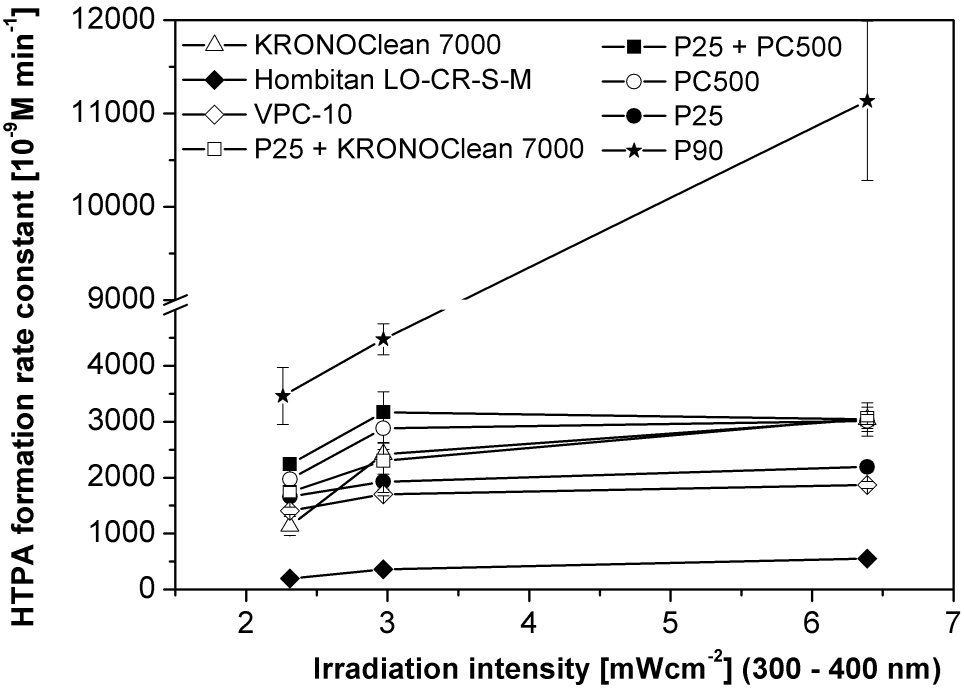

Figure 5: HTPA formation constants as a function of UV radiation intensities for different photocatalysts. In contrast to all other photocatalytic layers, P90 layer exhibits linear increase of HTPA formation, constant through the entire UVA intensity range.

tocatalytic activity. We believe that this seems to be the case with immobilized photocatalytic nanoparticles, which are more or less agglomerated and, despite smaller particles and higher BET surface area, do not offer better contact with the adsorbed organic coating of TPA. To confirm this, results of P90 should be considered, where higher photocatalytic activity was achieved with BET < 170 m^2g^{-1}. Thus, it can be concluded that BET surface effects photocatalytic activity only to some extent and since it is reported that there is no synergy between anatase and rutile [18], other properties, such a nanostructure, influence photocatalytic activity significantly. It is reported [24, 25] that Anatase TiO_2 with well defined faces showed higher activity and decahedral anatase with particle width of ca. 40 nm showed excellent activity because of the optimized balance between efficient separation of redox sites and large specific surface area [26]. However, this can not be easily concluded while there are many different factors we don't know that can effect photocatalytic activity [20].

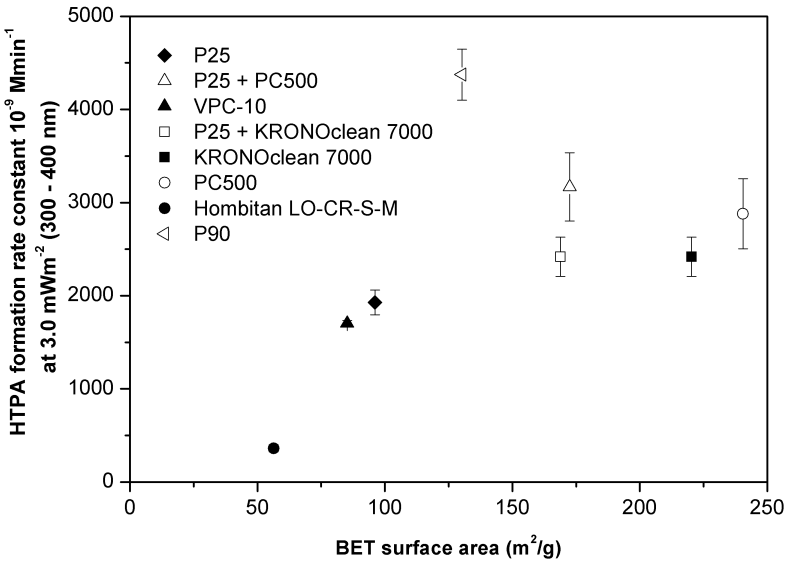

Figure 6: HTPA formation constants presented as a function of BET surface area of different photocatalysts. Irradiation intensity in Suntest was 287 Wm^{-2}, which corresponds to 3.0 mW/cm^2 of UVA.

4. Conclusions

We tested photocatalytic activity of five commercially available TiO_2 photocatalysts (P25, P90, PC500, KRONOClean 7000, VPC-10), one pigment (Hombitan LO-CR-S-M) and two mixtures (P25+PC500, P25+KRONOClean 7000), which were successfully immobilized on glass slides by sol suspension procedure. Despite lower BET surface area (130 m^2g^{-1}) in comparison to optimal BET ($\approx$170 m^2g^{-1}) for immobilized photocatalyst (Figure 6), Aeroxide® P90 incorporated in to the binder indicates the most photocatalytically active layer (Figure 5) and linear photocatalytic activity through out all ranges of irradiation intensities (2.3 mW/cm^2 - 6.4 mW/cm^2). From this result, it could be concluded that superior photocatalytic activity of P90 photocatalyst originates from its nanostrusture and consequently beter charge separation, so that more intensive recombination of positive h^+ and photoexcited e^- occur at much higher UVA irradiation intensities in comparison to other tested photocatalyst. However this was not proven. Due to its photocatalytic activity, P90 will be used further as a fixed phase in water photocatalytic reactor.

5. Acknowledgements

We are grateful to Betka Goličič and dr. Urh Černigoj from R&D department of BIA Separations for BET analysis and to dr. Egon Pavlica from Laboratory of Organic Matter Physics - University of Nova Gorica for performing the AFM analysis. This work has been financially supported by the Electrolux S.P.A. and Slovenian Research Agency.

6. References

[1] L. Zhang, R. Dillert, D. Bahnemann, and M. Vormoor. Photo-induced hydrophilicity and self-cleaning: models and reality. *Energy & Environmental Science*, 5:7491 – 7507, 2012.

[2] C. Akly, P. A. Chadik, and D. W. Mazyck. Photocatalysis of gas-phase toluene using silica-titania composites: Performance of a novel catalyst immobilization technique suitable for large-scale applications. *Applied Catalysis B: Environmental*, 99(1-2):329 – 335, 2010.

[3] M. Tasbihi, M. Kete, A. M. Raichur., N. N. Tušar, and U. L. Štangar. Photocatalytic degradation of gaseous toluene by using immobilized titania/silica on aluminum sheets. *Environmental Science and Pollution Research*, 19:3735–3742, 2012.

[4] A. Folli, C. Pade, T. B. Hansen, T. De Marco, and D. E. Macphee. TiO_2 photocatalysis in cementitious systems: Insights into self-cleaning and depollution chemistry. *Cement and Concrete Research*, 42(3):539 – 548, 2012.

[5] X. Zhu, M. A. Nanny, and E. C. Butler. Photocatalytic oxidation of aqueous ammonia in model gray waters. *Water Research*, 42(10-11):2736 – 2744, 2008.

[6] M. Sanchez, M.J. Rivero, and I. Ortiz. Photocatalytic oxidation of grey water over titanium dioxide suspensions. *Desalination*, 262(1-3):141 – 146, 2010.

[7] S. Malato, P. Fernandez-Ibanez, M.I. Maldonado, J. Blanco, and W. Gernjak. Decontamination and disinfection of water by solar photocatalysis: Recent overview and trends. *Catalysis Today*, 147(1):1 – 59, 2009.

[8] F. Sciacca, J. A. Rengifo-Herrera, J. Wethe, and C. Pulgarin. Solar disinfection of wild salmonella sp. in natural water with a 18L CPC photoreactor: Detrimental effect of non-sterile storage of treated water. *Solar Energy*, 85(7):1399 – 1408, 2011.

[9] Luigi Rizzo. Inactivation and injury of total coliform bacteria after primary disinfection of drinking water by TiO_2 photocatalysis. *Journal of Hazardous Materials*, 165(1-3):48 – 51, 2009.

[10] G. E. Imoberdorf, G. Vella, A. Sclafani, L. Rizzuti, O. M. Alfano, and A. E. Cassano. Radiation model of a TiO_2-coated, quartz wool, packed-bed photocatalytic reactor. *AIChE Journal*, 56(4):1030–1044, 2010.

[11] G. Plesch, M. Vargova, U.F. Vogt, M. Gorba, and K. Jesenak. Zr doped anatase supported reticulated ceramic foams for photocatalytic water purification. *Materials Research Bulletin*, 47(7):1680 – 1686, 2012.

[12] A. Y. Shan, T. I. M. Ghazi, and S. A. Rashid. Immobilisation of titanium dioxide onto supporting materials in heterogeneous photocatalysis: A review. *Applied Catalysis A: General*, 389(1-2):1 – 8, 2010.

[13] D. Peng, T. J. Carneiro, A. J. Moulijn, and G. Mul. A novel photocatalytic monolith reactor for multiphase heterogeneous photocatalysis. *Applied Catalysis A: General*, 334(1-2):119 – 128, 2008.

[14] A. Šuligoj, U. Černigoj, and L. U. Štangar. Preparation procedure of durable titania coatings on metal supports for photocatalytic cleaning applications. *The Slovenian Intellectual Property Office*, National patent application number P-201000432, 2010.

[15] U. Černigoj, M. Kete, and U. L. Štangar. Development of a fluorescence-based method for evaluation of self-cleaning properties of photocatalytic layers. *Catalysis Today*, 151(1-2):46 – 52, 2010.

[16] A. Mills, C. Hill, and P. K.J. Robertson. Overview of the current ISO tests for photocatalytic materials. *Journal of Photochemistry and Photobiology A: Chemistry*, 237(0):7 – 23, 2012.

[17] J. Krysa, M. Keppert, G. Waldner, and J. Jirkovsky. Immobilized particulate TiO_2 photocatalysts for degradation of organic pollutants: Effect of layer thickness. *Electrochimica Acta*, 50(25-26):5255 – 5260, 2005.

[18] B. Ohtani, O.O. Prieto-Mahaney, D. Li, and R. Abe. What is degussa (Evonik) P25? Crystalline composition analysis, reconstruction from isolated pure particles and photocatalytic activity test. *Journal of Photochemistry and Photobiology A: Chemistry*, 216(2-3):179 – 182, 2010.

[19] R. G. Nair, S. Paul, and S.K. Samdarshi. High uv/visible light activity of mixed phase titania: A generic mechanism. *Solar Energy Materials and Solar Cells*, 95(7):1901 – 1907, 2011.

[20] B. Ohtani. Photocatalysis a to z - what we know and what we do not know in a scientific sense. *Journal of Photochemistry and Photobiology C: Photochemistry Reviews*, 11(4):157 – 178, 2010.

[21] C. B. Almquist and P. Biswas. Role of synthesis method and particle size of nanostructured TiO_2 on its photoactivity. *Journal of Catalysis*, 212(2):145 – 156, 2002.

[22] H. Lin, C.P. Huang, W. Li, C. Ni, S. Ismat Shah, and Y.-H. Tseng. Size dependency of nanocrystalline TiO_2 on its optical property and photocatalytic reactivity exemplified by 2-chlorophenol. *Applied Catalysis B: Environmental*, 68(1-2):1 – 11, 2006.

[23] S. Brosillon, L. Lhomme, C. Vallet, A. Bouzaza, and D. Wolbert. Gas phase photocatalysis and liquid phase photocatalysis: Interdependence and influence of substrate concentration and photon flow on degradation reaction kinetics. *Applied Catalysis B: Environmental*, 78(3-4):232 – 241, 2008.

[24] A. Fumiaki, O.-O. Prieto-Mahaney, T. Yoshihiro, T. Yasumoto, T. Shibayama, and B. Ohtani. Decahedral single-crystalline particles of anatase titanium(iv) oxide with high photocatalytic activity. *Chemistry of Materials*, 21(13):2601–2603, 2009.

[25] N. Sugishita, Y. Kuroda, and B. Ohtani. Preparation of decahedral anatase titania particles with high-level photocatalytic activity. *Catalysis Today*, 164(1):391 – 394, 2011.

[26] N. Murakami, S. Kawakami, T. Tsubota, and T. Ohno. Dependence of photocatalytic activity on particle size of a shape-controlled anatase titanium(iv) oxide nanocrystal. *Journal of Molecular Catalysis A: Chemical*, 358(0):106 – 111, 2012.

Characterization of hydrophobicity of chromatographic monolithic columns

Mateja Simonič

BIA Separations d.o.o., Mirce 21, SI-5270 Ajdovščina

Abstract

The objective of this study was to develop chromatographic method for determination of hydrophobicity of the chromatographic columns. Hydrophobicity of test set of columns with different ligand chemistry and density was evaluated. Chemical structure of custom made CIM monoliths was investigated with Infrared Spectroscopy and hydrophobicity of the polymer was evaluated with Contact Angle Measurement. Separation of mixture of uracil, lysozyme and α-chymotrypsinogen A under Hydrophobic Interaction Chromatography conditions gave good correlation of retention time with contact angle values which correspond to degree of hydrophobicity. Moreover, since poor recovery was observed on some columns, Hydrophobic Interaction Chromatography was coupled with Reversed Phase Chromatography in order to elute whole amount of sample from the column.

Keywords: Hydrophobicity, RPC, HIC, Monoliths, Proteins

Introduction

Nonspecific adsorption of the sample species on the surface of chromatographic stationary phase presents a significant problem in applications using chromatographic methods in purification processes since it causes clogging of the stationary phase. The origin of this nonspecific sample binding are the proteins that bind to resins based on physical adsorption which is due to hydrophobic interactions [1]. This is the reason why the tendency to make more hydrophilic surface of the columns is increasing

Email address: mateja.simonic@monoliths.com (Mateja Simonič)

[2]. The most common way to increase hydrophilicity of novel chromatographic support is to make a hydrophilic coating on their surface.

When developing new chromatographic stationary phases, researchers have to use various characterization methods to evaluate properties of the material. Evaluation methods for chromatographic supports can be divided into five categories: methods for determination of physico-chemical properties (particle size and shape, pore size, specific surface area etc.), spectroscopic techniques (IR and NMR), statistical methods for comparison of different phases with similar chromatographic properties, thermodynamic measurements that provide information on the thermodynamic driving forces during the chromatographic separations of the sample and chromatographic test methods [3].

Claessens et al. agreed that the last set of characterization methods is the most useful equipment when user is selecting proper column for specific experiments. Chromatographic methods were further subdivided into empirically based and model-based evaluation methods. Empirically based methods use carefully selected test molecules, which would show specific column property (silanol activity, hydrophobicity etc.). There are many empirically based methods for determination of hydrophobicity of reversed-phase chromatographic columns: Engelhardt test [4], Galushko test [5] etc. These tests use small aromatic molecules such as uracil, anthracene, derivatives of aniline etc.

Not only the hydrophobicity of stationary phases but also hydrophobicity of proteins has important role in nonspecific adsorption of the sample to the surface of the columns. Hydrophobicity of proteins has been investigated with chromatographic methods, especially with Hydrophobic Interaction Chromatography (HIC), which is widely used in downstream processing of proteins. Asenjo et al. are studying protein retention in HIC with several different theories [6]. Their simplest methodology for determination of protein hydrophobicity is using information about average surface hydrophobicity of proteins [6]. From that information they predicted the retention time of the protein and correlated it with experimental values. They also transferred this theory to the mixture of proteins and on the real sample from cell extract [8]. The second methodology uses classical thermodynamic model to calculate hydrophobic contact area of the proteins (contact area between the stationary phase and the protein). Results correlated well with the retention time for three out of four ribonucleases with similar average surface hydrophobicity [9]. The most sophisticated methodology uses molecular docking stimulations to investigate surface area of interactions between proteins and hydrophobic moiety on the chro-

matographic column [10]. The comparison between local hydrophobicity (average surface hydrophobicity of the interfacial zone) showed a high correlation with the hydrophobic contact area and with retention time. However, the studies were performed on few stationary phases using small set of proteins.

The effect of different stationary phase resin chemistry (different backbone and ligand) and protein physicochemical properties on protein binding in HIC using linear gradient chromatography and quantitative structure-retention relationship (QSRR) was investigated by Ladiwala and coworkers [11]. Influence of the ligand and backbone chemistry on the binding affinity was studied with comparison of the Butyl and Phenyl Sepharose and 650M columns. Phenyl Sepharose resin had stronger binding than Butyl, while 650M supports had comparable binding affinities. When examining the effect of backbone chemistry the protein retention on both butyl resins was comparable. For phenyl supports the binding affinity was stronger for Sepharose column. Researchers observed altering of the selectivity of separation with changing the ligand and/or backbone chemistry. The QSRR modeling provided good correlations between experimental and predicted data on training, validation and test sets of proteins.

Jennissen in his review article [12] describes a systematic approach to the purification of proteins via HIC. With increasing of the chain length of the ligand on the chromatographic support the strength of protein binding increased to very tight binding. Another optimizing parameter is surface density of ligands. Grading of hydrophobicity could be produced by simply increasing the density of ligands on the surface of the resin. With varying the surface concentration of ligands the sigmoidal function of amount of adsorbed protein is achieved. Sigmoidal functions show that surface density of ligands is minor for columns with longer chains.

As one can see from this short review of the literature, a lot of researchers are studying column hydrophobicity and protein hydrophobicity with various chromatographic methods. The objective of our study was to develop chromatographic method for evaluation of hydrophobicity of current and novel more hydrophilic Convective Interaction Media – CIM monolithic columns with test set of proteins, since small molecules are not the most appropriate samples for monolithic columns. CIM monoliths from BIA Separations d.o.o. proved to be the tool for fast, efficient and highly productive purification processes for large biomolecules [13, 14]. As monoliths are mainly used for the separation and purification of proteins, pDNA and viruses the best way for their characterization is to use methods and samples that are similar to the real samples.

Determination of column hydrophobicity was very similar to the method from Tosoh Corporation [16], where they separated mixture of three proteins under HIC conditions on resins with different hydrophobicities. Some changes were done due to optimization of the method for monolithic columns. We used CIM Epoxy, CIM Hydroxy and custom made Butyl and Phenyl monoliths with different ligand density on the surface (25, 50, 75 and 100%). These columns are hydrophobic columns and they served as a test set for development of the method, which could be used in future for novel more hydrophilic columns. In some cases poor recovery of proteins was obtained under HIC conditions. However, we were able to elute proteins with almost 100% recovery by coupling of HIC and RPC methods.

1. Characterization experiments

1.1. Materials

Sodium hydroxide, acetonitrile (ACN), 2-propanol and α-chymotrypsinogen A from bovine pancreas were purchased from Sigma-Aldrich (St. Louis, MO, USA). Lysozyme from chicken egg white, trifluoroacetic acid (TFA) and uracil were purchased from Fluka (now part of Sigma-Aldrich). Ammonium sulfate (AS) was obtained from Merck (Darmstadt, Germany) and sodium dihydrogen phosphate-2-hydrate from Honeywell (Seelze, Germany). All water solutions were prepared using purified water and were filtered through a 0,22μm PES filter (TPP, Trasadingen, Switzerland). Acetonitrile was already purchased HPLC grade. Sample solutions for injection on columns were filtered through syringe filters with pore size 0,45μm (Macherey-Nagel, Düren, Germany). All 1 mL CIM columns for this research were custom made by BIA Separations d.o.o. (Ajdovščina, Slovenia). Flat and nonporous special disks were polymerized from the monomeric mixture with the same molar ratio between monomers as in mixture for polymerization of monoliths. The only difference was that the monomeric mixture for nonporous disks had no porogens.

1.2. Methods

1.2.1. Infrared spectroscopy

Chemical structure of chromatographic columns was obtained with Infrared spectroscopy. A sample of monolith was grinded and pressed over the ATR diamond of the ATR-FTIR spectrometer [1]. The spectrum was

[1] ATR-FTIR spectrometer Spectrum Two, Spectrum 10 software (Perkin Elmer, Massachusetts, USA

recorded at highest possible absorption intensity of IR bands, what was regulated with the adjustment of the pressure on the ATR diamond. Spectra was collected from 4000 to 450 cm^{-1}.

1.2.2. Contact angle measurement

Contact angle measurements were obtained on Contact Angle Meter CAM-100 [2]. The contact angle was calculated by software fitting of water drop curvature on the surface of the flat and nonporous samples. The drop shape is analyzed by observing the drop from the side. Samples for contact angle measurement have to be flat and nonporous otherwise the water penetrates into pores. Constant volume of water drop was assured by constant distance between the end of the needle of the syringe full of water and surface of disks. Contact angle of one water drop was measured three times in a row and three drops were measured per sample in that manner. In that manner we were able to obtain average value of contact angle for samples which correspond to the value of hydrophobicity of the sample.

1.2.3. Hydrophobic Interaction Chromatography - HIC

Separation of proteins under HIC conditions were performed using a gradient HPLC system Smartline (Knauer, Berlin, Germany) consisting of two Knauer Smartline Pump 1050, an injection valve with 200 μL sample loop, a Knauer UV-VIS absorbance detector model K-2500 with a 3 mm optical path cell and a conductivity monitor (Amersham Biosciences, GE Healthcare, Uppsala, Sweden), all connected via a Knauer interface box to a personal computer for real time data acquisition by ChromGate 3.3.2. software.

Gradient elution HIC experiments with mixture of uracil, lysozyme and α-chymotrypsinogen A were performed at flow rate 8 ml/min using a decreasing salt gradient in 20 column volumes (CV) from 100% buffer A (2 M $(NH_4)_2SO_4$ and 0,1 M $NaH_2PO_4 \cdot 2\,H_2O$, pH 7,0) to 100% buffer B (0,1 M $NaH_2PO_4 \cdot 2\,H_2O$, pH 7,0). Mixture of samples was prepared from stock solution. Final solution contained 0,06 mg/mL uracil, 0,8 mg/mL lysozyme and 0,8 mg/mL α-chymotrypsinogen A in 1,6 M $(NH_4)_2SO_4$ and 0,1 M $NaH_2PO_4 \cdot 2\,H_2O$.

HIC experiments coupled with RPC experiments were performed at flow rate 5 ml/min using the same decreasing salt gradient. After 7,5 CV of 100 % buffer B at the end of chromatographic method the pumps were

[2] KSV Instrument Ltd, Helsinki, Finland

stopped and changing of mobile phase B from buffer B to H_2O was done. After 42,5 CV of washing with H_2O the column was moved to other HPLC system where RPC experiments were carried out. Each sample was diluted in 1,6 M $(NH_4)_2SO_4$ and 0,1 M $NaH_2PO_4 \cdot 2\,H_2O$. Uracil was saturated and ten times diluted in buffer B. Then 4 M AS was added to achieve final concentration of AS. The concentration of proteins in 1,6 M AS was 1 mg/mL.

1.2.4. Reversed Phase Chromatography - RPC

RPC experiments were done on a gradient HPLC system (Knauer, Berlin, Germany) consisting of two Knauer Type 64 analytical pumps, an injection valve with 200 μL sample loop and a Knauer UV-VIS absorbance detector model VWM with a 10 mm optical path cell. All parts were connected via a Knauer interface box to a personal computer for real time data acquisition by Eurochrom 2000 software.

RPC experiments after the HIC step were performed at flow rate 5ml/min using the same increasing acetonitrile gradient in 20 CV from 100% buffer A (5% ACN with 0,15% TFA) to 100% buffer B (90% ACN with 0,15% TFA). Starting step in method for coupled experiments was 2,5 CV of H_2O and 5 CV of buffer A.

For recovery calculations we loaded the same amount of the sample solutions on the HPLC systems without and with the column. From these measurements surface area of the peaks were obtained. The recovery was measured as the ratio between peak area of protein eluted from the column and peak area of the protein which was not loaded on the column. The same sample solutions in 1,6 M $(NH_4)_2SO_4$ and 0,1 M $NaH_2PO_4 \cdot 2H_2O$ were used for HIC and RPC experiments.

Regeneration of the columns was performed after each chromatographic run by washing them with 20 CV of water, 10 CV of 2-propanol (incubation for 1 hour), 30 CV of water, 10 CV of 1M NaOH (incubation for 2 hours) and final washing step with 30 CV of water.

2. Results and discussion

2.1. Characterization of novel monoliths

Since monoliths with various ligand densities were prepared for the first time for this research, their characteristics were first tested.

2.1.1. Infrared Spectroscopy

Molecular structure of polymeric material was verified with IR spectroscopy. CIM Epoxy monoliths are made from poly(glycidyl methacrylate-co-ethylene dimethacrylate) (also referred to as poly(GMA-co-EDMA)), which contains epoxy groups as ligands on the surface of material. Epoxy group has characteristic absorption peaks in IR spectra at approximately 850 and 910 cm^{-1} (Figure 1(a)).

For polymerization of butyl and phenyl monoliths with various ligand densities different ratios (25, 50, 75 and 100%) between butyl or phenyl and epoxy groups were used. ATR-FTIR spectroscopy can not be used as a quantitative method, but decreasing of the ratio between epoxy and methacrylate carbonyl vibration at 1730 cm^{-1} (data not shown) is observed with increasing concentration of butyl groups in the sample (Figure 1 (a)). It does not serve as a direct proof of the inclusion of butyl groups within the monolith. These results were expected because butyl groups substitutes epoxy groups in the polymer and 100% Butyl correspond to a monolith with no epoxy groups present.

Similar behavior is present in IR spectra of Phenyl monoliths (Figure 1 (b)). Moreover, decreasing of epoxy vibrations correlates with the increase of a band with absorption maximum at approximately 700 cm^{-1}, which originates from phenyl ligand. This peak originates from vibrations of C-H bonds in aromatic ring [17].

Different ligand densities in monoliths were confirmed with these results. That meant that we probably made columns with various hydrophobicity [12]. The next step was determination of actual hydrophobicity of prepared nonporous samples.

2.1.2. Contact angle measurement

Contact angle measurement (CAM) is common method for determination of hydrophobicity of the material [18]; in our study for determination of hydrophobicity of novel monoliths. CAM is believed to be the simplest method for determination of solid-vapor and solid-liquid interfacial tensions [19]. It is easily performed by establishing the tangent of a liquid drop with a solid surface at the base.

The problem of applying this method on CIM monoliths is the porosity of the material, which disables direct measurements of contact angles. In order to overcome the problem flat and nonporous special disks were prepared. Monomeric mixture for polymerization of these disks had the same molar ratio between monomers as it was used for the polymerization of monoliths. The only difference was that the monomeric mixture

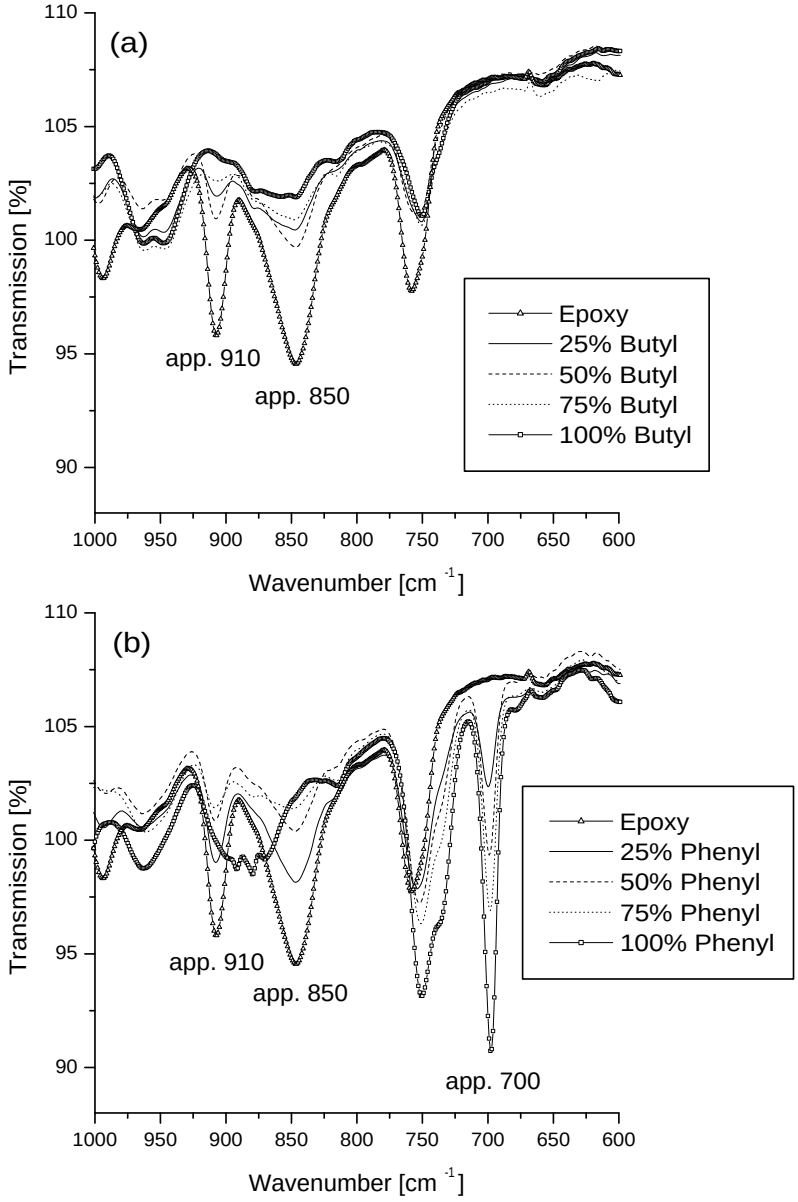

Figure 1: IR spectra of (a) Epoxy and Butyl monoliths and (b) Epoxy and Phenyl monoliths with various ligand densities. Scale from 1000 to 600 cm^{-1}.

for nonporous disks had no porogens. In that manner appropriate samples were prepared and contact angle was successfully measured. On every sample three drops of water were measured and for every drop three measurements were done. The average of this nine results was calculated. Measurement was done on the reference material in order to obtain measurements error: $86,2^\circ \pm 2,8^\circ$.

In Figure 2, increasing values of contact angle with increasing ligand densities can be observed for both Butyl and Phenyl set. This means that hydrophobicity is increasing. Epoxy sample is more hydrophobic than Hydroxy and more hydrophilic than Butyl and Phenyl samples.

When comparing both lines of monoliths there is no constant difference between samples with the same ligand density. For 25% and 100% samples it is observed that butyl samples are more hydrophobic than phenyl (differences in contact angle results are $3,6^\circ$ and $5,1^\circ$, respectively), but for 50% and 75% samples the values are quite similar. When comparing these results we have to bear in mind, that nonporous samples might not be perfectly flat. There may be some irregularities on the surface which could be the reason for slightly unexpected contact angles.

The results confirmed different hydrophobicity of novel monoliths with various ligand density of butyl and phenyl groups. Those results were important basis for our further work, since we wanted study a retention of test set of molecules on chromatographic columns with various hydrophobictiy.

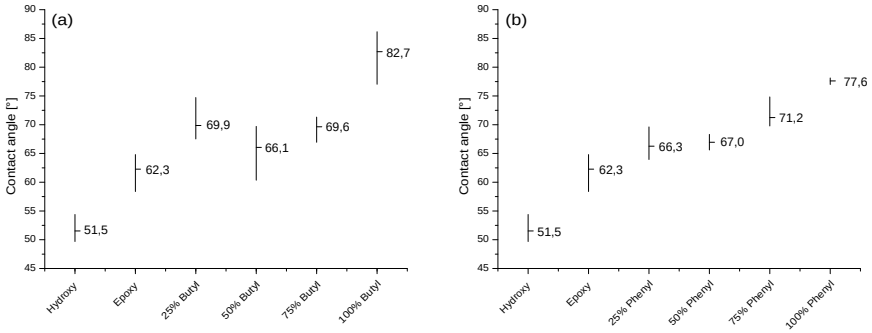

Figure 2: Contact angles of (a) Hydroxy, Epoxy and Butyl line samples and (b) Hydroxy, Epoxy and Phenyl line samples. Average value of nine measurement is marked with horizontal line, error bars represent values of those nine measurements.

2.2. Hydrophobic interaction chromatography

The main part of our study was to develop chromatographic method for evaluation of hydrophobicity of monoliths with proteins. Determination of hydrophobicity was very similar to the method from Tosoh Corporation [16]. In their study ribonuclease A, lysozyme and α-chymotrypsinogen A with concentration 1 mg/mL were used. In our experiments we replaced ribonuclease A with small molecule uracil in order to monitor pulse response in every chromatographic run. Pulse response gives information about flow profile through the column. If there are some irregularities in a flow pattern, chromatogram shows a pronounced fronting or tailing of the peak of molecule under nonbinding conditions [20]. The flow rate was changed from 1 to 8 ml/min as well. Other chromatographic parameters are described in Section 1.2.3.

As it is evident from Figure 3 uracil was a very good probe for pulse response since it eluted in flow through step in case of all the columns. Lysozyme eluted at higher ammonium sulfate concentration than α-chymotrypsinogen A in case of every column in the research. This confirms that lysozyme is more hydrophilic protein than α-chymotrypsinogen A. Comparison of chromatograms for Epoxy and Hydroxy monoliths (Figure 3 (a) and Table 1) shows that lysozyme elutes at similar salt concentration from both columns, while α-chymotrypsinogen A elutes first from Hydroxy column. It is proposed that some additional interactions are present between hydroxy groups on the surface of the column and lysozyme.

Table 1: Conductivity values of elution peaks for lysozyme and α-chymotrypsinogen A for studied monoliths. Values for 75% and 100% Phenyl are not shown.

Column	**Lysozyme conductivity** [%]	**α-Chymotrypsinogen A conductivity** [%]
Hydroxy	96	86
Epoxy	98	82
25% Butyl	63	37
50% Butyl	61	12
75% Butyl	67	18
100% Butyl	47	-
25% Phenyl	71	51
50% Phenyl	52	16

Separations of sample mixture on Butyl line monoliths (Figure 3 (a)) shows that Butyl monoliths are more hydrophobic than Epoxy and Hy-

droxy since proteins elute at lower ammonium sulfate concentration. Elution concentration of antichaotropic salt for protein peaks in case of 25%, 50% and 75% Butyl monoliths are not in good correlation with ligand density. It was expected that monoliths with higher ligand density would be more hydrophobic. Chromatogram for 100% Butyl shows that lysozyme elutes from the column in broad peak, while α-chymotrypsinogen A does not elute at all.

Monoliths from Phenyl line show excellent correlation between ligand density and salt concentration (Figure 3 (b)). With increasing percentage of ligands present on the surface of the column, hydrophobicity of the columns is increasing. Unfortunately, 75% and 100% Phenyl monoliths have broad peaks and poor recovery.

Comparison of protein retention for Butyl and Phenyl monoliths (Table 1) with the same ligand density shows that 25% Butyl is more hydrophobic than 25% Phenyl. But for 50% and 75% monoliths the trend is reversed. In [11] it was observed that Butyl and Phenyl Toyopearl 650M resins had comparable binding affinities to proteins. CIM monoliths and 650M resins could be compared since having the same backbone chemistry, but we do not know exact ligand density of the latter.

Since both methods, contact angle measurement and Hydrophobic Interaction Chromatography, give information about hydrophobicity of the material, those results were compared in Figure 4. For Butyl monoliths with ligand densities from 25% to 75% (Figure 4 (a)) it can be observed that elution of both proteins have similar trend - the maximum retention time is reached with 50% Butyl, which is not in correlation with contact angle. At this point we have to remember that nonporous disks for contact angle measurements were prepared without porogens and that could be the reason for slightly different properties due to different orientation of monomers on the surface of material. In case of 100% Butyl good correlation of two methods can be observed since it has maximum values for retention time and contact angle.

Figure 4 (b) shows good correlation between hydrophobicity and ligand density for 25% and 50% Phenyl monoliths. Data for 75% and 100% is not given since broad peaks can be observed in Figure 3 (b).

Poor recovery of proteins on some columns was observed during HIC experiments with mixture of proteins. That was the reason for repeating similar experiments with single samples (experimental data in 1.2.3). Recovery of uracil was 100% for every monolith used (data not shown) since it does not bind to the material in 2 M ammonium sulfate.

As one can see in Table 2 the recovery of proteins is dropping with

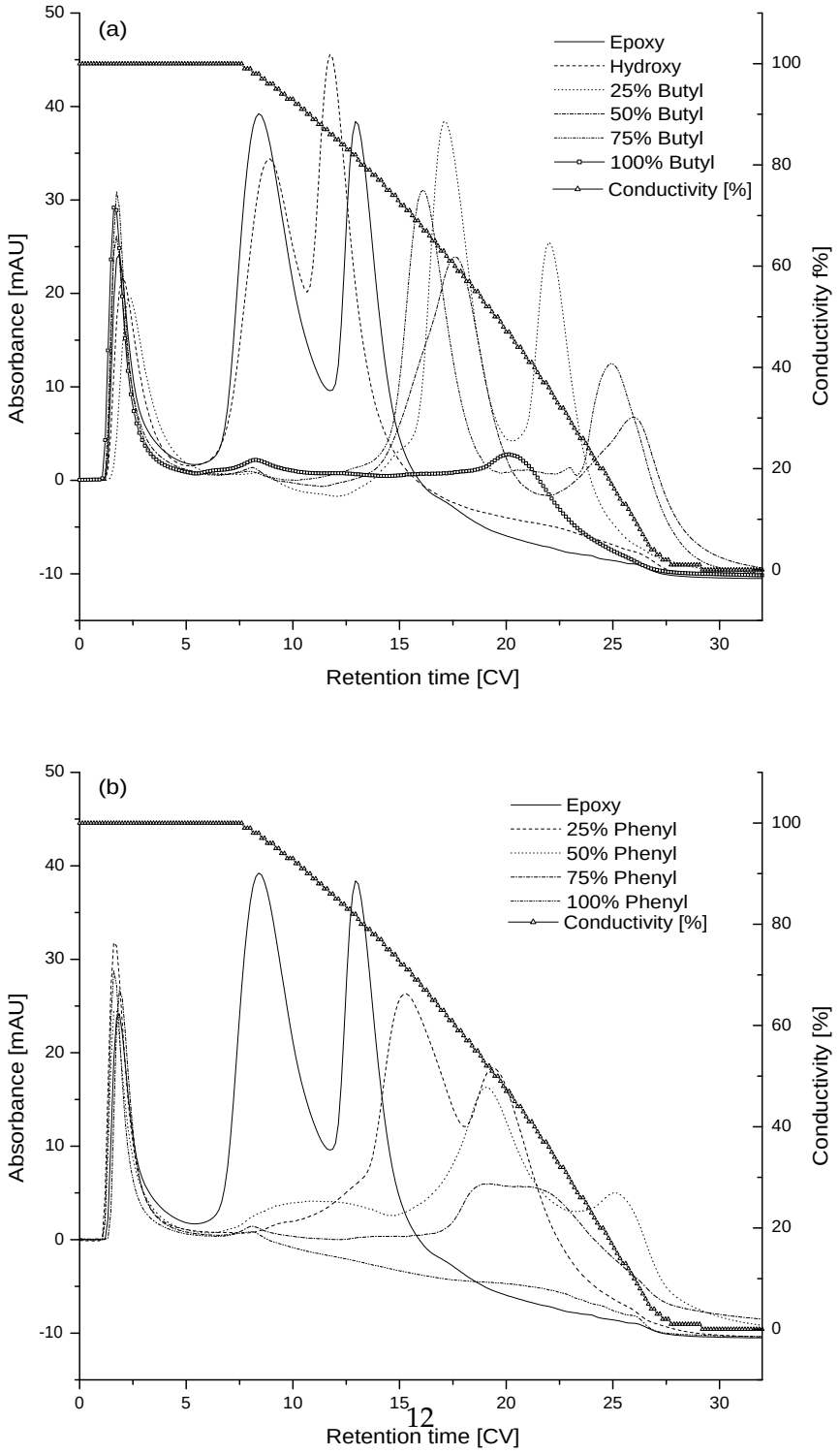

Figure 3: Chromatograms of mixture of uracil, lysozyme and α-chymotrypsinogen A on (a) Epoxy, Hydroxy and Butyl monoliths and (b) Epoxy and Phenyl monoliths.

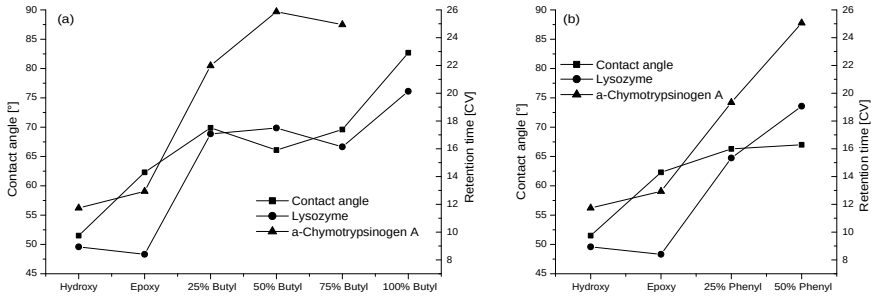

Figure 4: Comparison of contact angle and retention time for elution of proteins lysozyme and α-chymotrypsinogen A on (a) Hydroxy, Epoxy and Butyl line of monoliths and (b) Hydroxy, Epoxy and Phenyl monoliths. Data is not shown for 75% and 100% Phenyl monoliths because of broad peaks.

increasing ligand density or hydrophobicity. 100% Butyl, 75% and 100% Phenyl exhibit no recovery at all. In Figure 3 some elution of proteins could be observed on those columns. It is proposed that this difference is due to usage of samples with single protein.

Table 2: Recovery of lysozyme and α-chymotrypsinogen A under HIC conditions.

Column	**Lysozyme recovery** [%]	**α-Chymotrypsinogen A recovery** [%]
Hydroxy	101	101
Epoxy	96	104
50% Butyl	94	89
100% Butyl	0	0
25% Phenyl	93	92
50% Phenyl	89	91
75% Phenyl	0	0
100% Phenyl	0	0

2.2.1. Coupled chromatographic experiments

For regeneration step of columns after chromatographic runs 2-propanol was used, which denatures proteins and washes nonspecifically bound proteins from the surface of the column. This organic solvent was origin of the idea to use Reversed Phase Chromatography (RPC), which is based

on using organic modifiers such as acetonitrile, methanol, 2-propanol etc. [21]. RPC depends on the hydrophobic binding interaction between the solute molecule and the ligand on the surface of stationary phase, which is similar to interactions in HIC.

The idea was to couple HIC and RPC one after another. This would enable monitoring of the elution of proteins under different chromatographic conditions on the same column. Columns used for HIC-RPC experiments were those with poor recovery of proteins under HIC conditions; 100% Butyl, 50%, 75% and 100% Phenyl. The column was attached to the HPLC system with HIC mobile phases and the sample solution was loaded. After the chromatographic run (gradient elution with decreasing concentration of ammonium sulfate and washing step with water) the column was transferred to another HPLC system with RPC mobile phase. Very important step between HIC and RPC was washing of the column with excess of water in order to prevent clogging of the system due to precipitation of ammonium sulfate in acetonitrile solution. No elution of proteins was observed during water steps. All chromatographic data are described in sections 1.2.3 and 1.2.4.

In table 3 one can see retention time in column volumes and protein recoveries of the each chromatographic method and their summary. Data is not shown for uracil since it was eluted with 100% recovery in HIC step from every column used.

In case of three columns (75% and 100% Phenyl and 100% Butyl) there was no elution of proteins under HIC conditions. But in the following RPC step proteins eluted with quite high recovery. The only exception is elution from 75% Phenyl column which exhibit only 48% of α-chymotrypsinogen A recovery.

50% Phenyl column is the only case, where proteins eluted in HIC and RPC step. Lysozyme and α-chymotrypsinogen A elute under HIC conditions with high recovery (89 and 91, respectively). After summing both HIC and RPC recovery almost 100% recovery is achieved.

With coupling of the Hydrophobic interaction chromatography and Reversed phase chromatography we were able to elute proteins from the columns with high degree of hydrophobicity with very good recovery. Also the coupling of two different chromatographic methods on the same columns was achieved without having any problems.

Table 3: Retention times and recoveries of lysozyme and α-chymotrypsinogen A under coupled HIC and RPC conditions.

Column	**Sample**	**Conditions**	**Retention time** $[CV]$	**Recovery** $[\%]$
100% Butyl	Lysozyme	HIC RPC	No elution. 14,7	- 88 SUM 88
	α-Chymotrypsinogen	HIC RPC	No elution. 15,8	- 89 SUM 89
50% Phenyl	Lysozyme	HIC RPC	17,2 15,2	89 8 SUM 97
	α-Chymotrypsinogen	HIC RPC	22,3 17,2	91 6 SUM 97
75% Phenyl	Lysozyme	HIC RPC	No elution. 14,8	- 91 SUM 91
	α-Chymotrypsinogen	HIC RPC	No elution. 17,4	- 48 SUM 48
100% Phenyl	Lysozyme	HIC RPC	No elution. 15,2	- 94 SUM 94
	α-Chymotrypsinogen	HIC RPC	No elution. 19,5	- 85 SUM 85

3. Conclusions

The aim of our research was to develop a chromatographic method for characterization of hydrophobicity of current and novel monoliths. With selecting appropriate conditions (Hydrophobic Interaction Chromatography) and sample molecules we were able to distinguish between columns with different hydrophobicity. In the future the method will be transferred to novel more hydrophilic columns. For evaluation of their properties some changes might be crucial, such as concentration of antichaotropic salt. The method could be useful for determination of hydrophobicity of ion-exchange chromatographic columns since influence of charges on separation of proteins under high salt concentration in HIC is negligible.

Acknowledgements

We thank Sandra Kontrec, Urška Vidic, Rok Oblak and Metka Stantič for providing CIM monolithic columns and nonporous samples and for their technical assistance. We are very grateful to Sašo Plevčak, Mirjan Žorž and Jana Vidič for fruitful discussions. We gratefully acknowledge to Marko Kete and prof. dr. Urška Lavrenčič Štangar from the Laboratory for Environmental Research at University of Nova Gorica for enabling contact angle measurements.

References

[1] T. Shiyama, M. Furuya, A. Yamazaki, T. Terada, A. Tanaka, Bioorg. Med. Chem. 12 (2004) 2831.

[2] A. Maruška, O. Kornyšova, J. Biochem. Biophys. Methods 59 (2004) 1.

[3] H.A. Claessens, M.A. van Straten, C.A. Cramers, M. Jezierska, B. Buszewski, J. Chromatogr. A 826 (1998) 135.

[4] H. Engelhardt, M. Jungheim, Chromatographia 29 (1990) 59.

[5] S.V. Galushko, Chromatographia 36 (1993) 39.

[6] A. Mahn, J.A. Asenjo, Biotechnol. Adv. 23 (2005) 359.

[7] M.E. Lienqueo, A. Mahn, J.A. Asenjo, J. Chromatogr. A 978 (2002) 71.

[8] M.E. Lienqueo, A. Mahn, L. Vasquez, J.A. Asenjo, J. Chromatogr. A 1009 (2003) 189.

[9] A. Mahn, M.E. Lienqueo, J.A. Asenjo, J. Chromatogr. A 1043 (2004) 47.

[10] A. Mahn, G. Zapata-Torres, J.A. Asenjo, J. Chromatogr. A 1066 (2005) 81.

[11] A. Ladiwala, F. Xia, Q. Luo, C.M. Breneman, S.M. Cramer, Biotechnol. Bioeng. 93 (2006) 836.

[12] H.P. Jennissen, Nature Encyclopedia of Life Sciences 9 (2002) 353.

[13] J. Urthaler, R. Schlegl, A. Podgornik, A. Štrancar, A. Jungbauer, R. Necina, J. Chromatogr. A 1065 (2005) 93.

[14] P. Gagnon, BioProcess Int. 8 (2010) 22.

[15] T.B. Tennikova, J. Reusch, J. Chromatogr. A 1065 (2005) 13.

[16] Hydrophobic Interaction Chromatography brochure, Tosoh Bioscience (http://www.go-jsb.com/media/file/PDF/B09P17A_HIC_small.pdf).

[17] P.J. Larkin, Infrared and Raman spectroscopy : principles and spectral interpretation, Elsevier, Amsterdam, 2011.

[18] C.N.C. Lam, R. Wu, D. Li, M.L. Hair, A.W. Neumann, Adv. Colloid Interface Sci. 96 (2002) 169.

[19] D.Y. Kwok, A.W. Neumann, Adv. Colloid Interface Sci. 81 (1999) 167.

[20] A. Podgornik, J. Vidič, J. Jančar, N. Lendero, V. Frankovič, A. Štrancar, Chem. Eng. Technol. 28 (2005) 1435.

[21] Reversed Phase Chromatography, Principles and Methods, Amersham Biosciences (http://wolfson.huji.ac.il/purification/PDF/ReversePhase/AmershamRPCManual.pdf).

Evaluation of hikers' pro-environmental behaviour in Triglav National Park, Slovenia

Mojca Stubelj Ars

University of Nova Gorica, Center for Systems and Information Technologies, Vipavska 13, SI-5000 Nova Gorica

Abstract

To evaluate the pro-environmental behavior of visitors in the Alps, we surveyed 100 hikers on two hiking trails in Triglav National Park (TNP) in Slovenia, during the 2010 and 2012 summer seasons. We collected demographic data on hikers and examined 1) pro-environmental behavior at home, 2) willingness to pay for environmentally friendly goods and services, and 3) enrolment in environmental education and involvement in nature conservation projects. We identified 13 significant correlations between pro-environmental behavior questions and demographically based hikers groups. Level of education and enrolment in environmental educational activities predicted pro-environmental behavior and attitude toward nature conservation. Our results show that visitors who hike in TNP come in pairs or with friends, value nature, and are prepared to pay more for goods with eco-labels and services from environmentally responsible suppliers. Only 36.7% have enrolled in an educational program, training, workshop, or activity. The majority of respondents choose the location for their vacation based on an areas nature preservation characteristics. We discuss the factors that influence hikers pro-environmental behavior and investigate the relationship between level of education and hikers pro-environmental behavior at home. We also examine the importance of nature preservation characteristics in hikers choice of vacation destination. Finally, this research provides valuable data for understanding hikers behavior and suggestions for managers of protected area to create tourism offerings that are more educational and environmentally friendly.

Keywords: the Alps, pro-environmental behavior, nature conservation, hiking, protected area management

Email address: mojca.stubelj.ars@ung.si (Mojca Stubelj Ars)

Refer to: Stubelj Ars, M. 2013. Evaluation of hikers' pro-environmental behavior in Triglav National Park, Slovenia. eco.mont - Journal on Protected Mountain Areas Research and Management 5, 1. (Available at http://hw.oeaw.ac.at/eco.mont as of 1st June 2013).